

# HADES RV Programme with HARPS-N at TNG

## V. A super-Earth on the inner edge of the habitable zone of the nearby M-dwarf GJ 625 <sup>★</sup>

A. Suárez Mascareño<sup>1,2,3</sup>, J. I. González Hernández<sup>1,3</sup>, R. Rebolo<sup>1,3,4</sup>, S. Velasco<sup>1,3</sup>, B. Toledo-Padrón<sup>1,3</sup>, L. Affer<sup>5</sup>, M. Perger<sup>6</sup>, G. Micela<sup>5</sup>, I. Ribas<sup>6</sup>, J. Maldonado<sup>5</sup>, G. Leto<sup>7</sup>, R. Zanmar Sanchez<sup>7</sup>, G. Scandariato<sup>7</sup>, M. Damasso<sup>8</sup>, A. Sozzetti<sup>8</sup>, M. Esposito<sup>9</sup>, E. Covino<sup>9</sup>, A. Maggio<sup>5</sup>, A. F. Lanza<sup>7</sup>, S. Desidera<sup>10</sup>, A. Rosich<sup>6</sup>, A. Bignamini<sup>11</sup>, R. Claudi<sup>10</sup>, S. Benatti<sup>10</sup>, F. Borsa<sup>12</sup>, M. Pedani<sup>13</sup>, E. Molinari<sup>13</sup>, J. C. Morales<sup>6</sup>, E. Herrero<sup>6</sup>, and M. Lafarga<sup>6</sup>

<sup>1</sup> Instituto de Astrofísica de Canarias, E-38205 La Laguna, Tenerife, Spain  
e-mail: jonay@iac.es

<sup>2</sup> Observatoire Astronomique de l'Université de Genève, Versoix, Switzerland  
e-mail: Alejandro.SuarezMascareno@unige.ch

<sup>3</sup> Universidad de La Laguna, Dpto. Astrofísica, E-38206 La Laguna, Tenerife, Spain

<sup>4</sup> Consejo Superior de Investigaciones Científicas, Spain

<sup>5</sup> INAF - Osservatorio Astronomico di Palermo, Piazza del Parlamento 1, 90134 Palermo, Italy

<sup>6</sup> Institut de Ciències de l'Espai (CSIC-IEEC), Campus UAB, Carrer de Can Magrans s/n, 08193 Cerdanyola del Vallés, Spain

<sup>7</sup> INAF - Osservatorio Astrofisico di Catania, via S. Sofia 78, 95123 Catania, Italy

<sup>8</sup> INAF - Osservatorio Astrofisico di Torino, via Osservatorio 20, 10025 Pino Torinese, Italy

<sup>9</sup> INAF - Osservatorio Astronomico di Capodimonte, Via Moiariello, 16, 80131 - NAPOLI

<sup>10</sup> INAF - Osservatorio Astronomico di Padova, Vicolo dell'Osservatorio 5, 35122, Padova, Italy

<sup>11</sup> INAF - Osservatorio Astronomico di Trieste, via Tiepolo 11, 34143, Trieste, Italy

<sup>12</sup> INAF - Osservatorio Astronomico di Brera, Via E. Bianchi 46, I-23807 Merate (LC), Italy

<sup>13</sup> Fundación Galileo Galilei - INAF, Rambla José Ana Fernández Pérez 7, E-38712 Breña Baja, TF - Spain

Revised April-2017

### ABSTRACT

We report the discovery of a super-Earth orbiting at the inner edge of the habitable zone of the star GJ 625 based on the analysis of the radial-velocity (RV) time series from the HARPS-N spectrograph, consisting in 151 HARPS-N measurements taken over 3.5 yr. GJ 625 b is a planet with a minimum mass  $M \sin i$  of  $2.82 \pm 0.51 M_{\oplus}$  with an orbital period of  $14.628 \pm 0.013$  days at a distance of 0.078 AU of its parent star. The host star is the quiet M2 V star GJ 625, located at 6.5 pc from the Sun. We find the presence of a second radial velocity signal in the range 74-85 days that we relate to stellar rotation after analysing the time series of Ca II H&K and H $\alpha$  spectroscopic indicators, the variations of the FWHM of the CCF and and the APT2 photometric light curves. We find no evidence linking the short period radial velocity signal to any activity proxy.

**Key words.** Planetary Systems — Techniques: radial velocity — Stars: activity — Stars: chromospheres — Stars: rotation — Stars: magnetic cycle — starspots — Stars: individual (GJ 625)

### 1. Introduction

The detection rate of potentially habitable Earth-like planets around M-dwarfs is rapidly increasing (Wright et al. 2016; Anglada-Escudé et al. 2016; Jehin et al. 2016; Gillon et al. 2017; Astudillo-Defru et al. 2017). Since years ago it has been clear that M-dwarfs are a shortcut to find earth-like planets and therefore several surveys have attempted to take advantage of their

low masses and closer habitable zones (Quirrenbach et al. 2012; Bonfils et al. 2013; Howard et al. 2014; Irwin et al. 2015; Berta-Thompson et al. 2015a; Affer et al. 2016; Suárez Mascareño et al. 2017a; Perger et al. 2017b). M-dwarfs have also proven to be difficult targets because of their stellar activity. The signals induced by the stellar rotation can easily mimic those of planetary origin (Queloz et al. 2001; Bonfils et al. 2007; Boisse et al. 2011; Robertson et al. 2014; Suárez Mascareño et al. 2015; Newton et al. 2016; Vanderburg et al. 2016; Suárez Mascareño et al. 2017a,b). For the case of M-dwarfs these signals tend to be comparable to those of rocky planets close to the habitable zone of their stars (Howard et al. 2014; Robertson et al. 2014; Suárez Mascareño et al. 2015; Newton et al. 2016; Suárez Mascareño et al. 2017b). The interpretation of the radial velocity curves of M-dwarfs is usually complicated even in the quietest of stars. Low mass stars are the most common type of stars, offering valuable complementary information on the formation mechanisms

<sup>★</sup> Based on: observations made with the Italian Telescopio Nazionale Galileo (TNG), operated on the island of La Palma by the INAF - Fundación Galileo Galilei at the Roche de Los Muchachos Observatory of the Instituto de Astrofísica de Canarias (IAC); photometric observations made with the robotic telescope APT2 (within the EXORAP program) located at Serra La Nave on Mt. Etna.; lucky imaging observations made with the Telescopio Carlos Sánchez operated on the island of Tenerife by the Instituto de Astrofísica de Canarias in the Spanish Observatorio del Teide.

of planetary systems. For instance giant planets at close orbits are known to be rare around M dwarfs (Endl et al. 2006), while low mass rocky planets appear to be more frequent (Bonfils et al. 2013; Dressing & Charbonneau 2013; Dressing et al. 2015).

Even with the large amount of confirmed exoplanets (Howard et al. 2009; Mayor et al. 2011; Howard et al. 2012) the number of rocky planets remains comparably small with only about a hundred known around M-dwarfs. This is mostly because most surveys – including the Kepler survey – have focused primarily in solar type and K-type stars. In the recent years many planetary systems have been reported hosting Neptune mass planets and super-Earths (Udry et al. 2007; Delfosse et al. 2013; Howard et al. 2014; Astudillo-Defru et al. 2015), and a rapidly increasing amount of Earth-mass planets (Mayor et al. 2009; Berta-Thompson et al. 2015b; Wright et al. 2016; Affer et al. 2016; Anglada-Escudé et al. 2016; Jehin et al. 2016; Suárez Mascareño et al. 2017a; Gillon et al. 2017). However the frequency of Earth-sized planets around M-dwarfs is still not well established. Several studies have attempted to quantify the abundance of rocky planets in close orbits and in the habitable zones of M-dwarfs, but the uncertainties are still large, making it important to continue adding new planets to the sample (Bonfils et al. 2013; Gaidos 2013; Kopparapu 2013).

We report the discovery of a super-Earth orbiting the nearby star GJ 625 on the inner edge of its habitable zone. The discovery is part of the HADES (HARPS-n red Dwarf Exoplanet Survey) radial velocity (RV) program with HARPS-N at the Telescopio Nazionale Galileo in La Palma (Spain). The HADES RV program is the result of a collaborative effort between the Italian Global Architecture of Planetary Systems (GAPS, Covino et al. (2013); Poretti et al. (2016)) Consortium, The Institut de Ciències de l’Espai de Catalunya (ICE), and the Instituto de Astrofísica de Canarias (IAC). The HADES team has previously discovered two super-Earth exoplanets of minimum masses of  $\sim 6.3$  and  $\sim 2.5 M_{\oplus}$  orbiting the early-type M-dwarf GJ 3998 (Affer et al. 2016).

GJ 625 is a bright ( $V = 10.17$  mag) low activity ( $\log_{10}(R'_{\text{HK}}) \sim -5.5$ ) M-dwarf located at a distance of 6.5 pc from the Sun (van Leeuwen 2007; Gaia Collaboration et al. 2016). Table 1 shows the stellar parameters. Its low activity combined with its long rotation period, of more than 70 days, makes it a very interesting candidate to search for rocky planets.

## 2. Data & Observations

### 2.1. Spectroscopy

The star GJ 625 is part of the HADES RV program (Affer et al. 2016) and has been extensively monitored since 2013. We have used 151 HARPS-N spectra taken over 3.5 yr. HARPS-N (Cosentino et al. 2012) is a fibre-fed high resolution echelle spectrograph installed at the Telescopio Nazionale Galileo in the Roque de los Muchachos Observatory (Spain). The instrument has a resolving power greater than  $R \sim 115\,000$  over a spectral range from  $\sim 380$  to  $\sim 690$  nm and has been designed to attain very high long-term radial-velocity precision. It is contained in a vacuum vessel to avoid spectral drifts due to temperature and air pressure variations, thus ensuring its stability. HARPS-N is equipped with its own pipeline providing extracted and wavelength-calibrated spectra, as well as RV measurements and other data products such as cross-correlation functions and their bisector profiles.

Most of the observations were carried out using the Fabry Perot (FP) as simultaneous calibration. The FP offers the pos-

Table 1: Stellar parameters of GJ 625

Parameter	GJ 625	Ref.
RA (J2000)	16:25:25.36	1
DEC (J2000)	+54:18:12.19	1
$\mu_{\alpha}$ ( $\text{mas yr}^{-1}$ )	432.13	1
$\mu_{\delta}$ ( $\text{mas yr}^{-1}$ )	-171.48	1
Distance [pc]	6.49	1
$m_B$	$11.80 \pm 0.16$	2
$m_V$	$10.17 \pm 0.04$	2
Spectral Type	M2	3
$T_{\text{eff}}$ [K]	$3499 \pm 68$	3
$[Fe/H]$	$-0.38 \pm 0.09$	3
$M_{\star}$ [ $M_{\odot}$ ]	$0.30 \pm 0.07$	3
$R_{\star}$ [ $R_{\odot}$ ]	$0.31 \pm 0.06$	3
$\log g$ (cgs)	$4.94 \pm 0.06$	3
$\log(L_{\star}/L_{\odot})$	$-1.894 \pm 0.170$	3
$\log_{10}(R'_{\text{HK}})$	$-5.5 \pm 0.2$	0
$P_{\text{rot}}$ (days)	$77.8 \pm 5.5$	0
$v \sin i$ ( $\text{km s}^{-1}$ )	$< 0.2^*$	3
Secular acc. ( $\text{m s}^{-1} \text{ yr}^{-1}$ )	0.03	4

**References:** 0 - This work, 1 - Gaia Collaboration et al. (2016), 2 - Høg et al. (2000), 3 -Maldonado et al. (2017), 4 - Calculated following Montet et al. (2014).

\* Calculated using the radius estimated by Maldonado et al. (2017) and our period determination.

sibility of monitoring the instrumental drift with a precision of  $10 \text{ cm s}^{-1}$  without the risk of contamination of the stellar spectra by the ThAr saturated lines (Wildi et al. 2010). While this is not usually a problem in G and K stars, the small amount of light collected in the blue part of the spectra of M-dwarfs might compromise the quality of the measurement of the Ca II H&K flux. The FP allows a precision of  $\sim 1 \text{ ms}^{-1}$  in the determination of the radial velocities of the spectra with highest signal to noise ratios while assuring the quality of the spectroscopic indicators even in those spectra with low signal to noise ratios. Those observations taken without the FP were taken without simultaneous lamp reference.

### 2.2. EXORAP photometry

Along with the HARPS-N spectra we have 2.6 yr of B, V, R, and I-band photometric data collected at the INAF-Catania Astrophysical Observatory with an 80 cm f/8 *Ritchey-Chretien* robotic telescope (APT2) located at Serra la Nave on the Mt. Etna. The data is reduced by overscan, bias, dark subtraction and flat fielding with IRAF<sup>1</sup> procedures and visually inspected to check the quality (see Affer et al. (2016) for details). Errors in the individual measurements are the quadratic sum of the intrinsic noise (photon noise and sky noise) and the RMS of the ensemble stars used for the differential photometry.

<sup>1</sup> IRAF is distributed by the National Optical Astronomy Observatories, which are operated by the Association of Universities for Research in Astronomy, Inc., under cooperative agreement with the National Science Foundation.

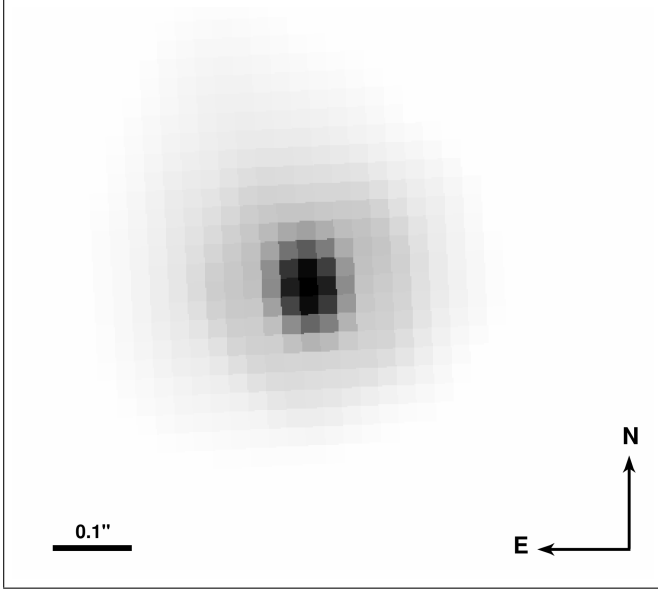


Fig. 1: Diffraction-limited image of GJ 625 after lucky imaging processing with a selection of the 30% best individual TCS/FastCam frames.

### 2.3. FastCam Lucky Imaging Observations

On June 6th 2016, we collected 50,000 individual frames of GJ 625 in the I band using the lucky imaging FastCam instrument (Oscos et al. 2008) at the 1.5m Carlos Sánchez Telescope in the Observatorio del Teide, Tenerife, with 30 ms exposure time for each frame. FastCam is an optical imager with a low noise EMCCD camera which allows to obtain speckle-featuring not saturated images at a fast frame rate (Labadie et al. 2011).

In order to construct a high resolution, diffraction limited, long-exposure image, the individual frames were bias subtracted, aligned and co-added using our own Lucky Imaging algorithm (Velasco et al. 2016). Figure 1 presents the high resolution image constructed by co-addition of the best percentage of the images using lucky imaging and shift-and-add algorithms. Due to the atmospheric conditions of the night, the selection of 30% of the individual frames was found to be the best solution to produce a deep and diffraction limited image of the target, resulting in a total integration time of 450 seconds. The combined image achieved  $\Delta m_I = 4.5 - 5.0$  at  $1''$ . We find no bright contaminant star in the diffraction limited image.

## 3. Determination of Stellar Activity Indicators and Radial Velocities

### 3.1. Activity Indicators

For the activity analysis we use the extracted order-by-order wavelength-calibrated spectra produced by the HARPS-N pipeline. For a given star, the change in atmospheric transparency from day to day causes variations in the flux distribution of the recorded spectra that are particularly relevant in the blue, where we intend to measure Ca II lines. In order to minimize the effects related to these atmospheric changes we create a spectral template for each star by de-blazing and co-adding every available spectrum and use the co-added spectrum to correct the order-by-order fluxes of the individual ones. We also correct each spectrum for the Earth's barycentric radial velocity and the radial velocity of the star using the measurements given by the

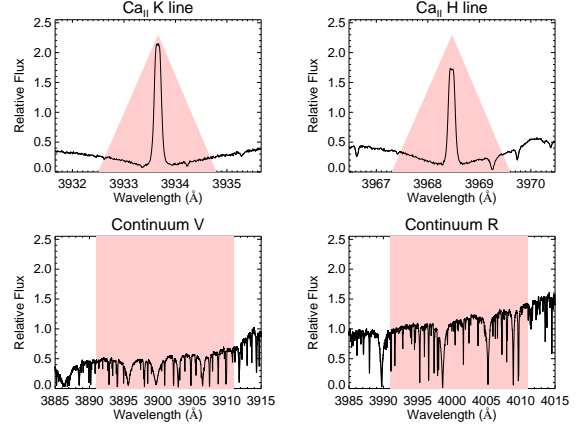


Fig. 2: Ca II H&K filter of the spectrum of the star GJ 625 with the same shape as the Mount Wilson Ca II H&K passband.

standard pipeline and re-binned the spectra into a wavelength-constant step. Using this HARPS-N dataset, we expect to have high quality spectroscopic indicators to monitor tiny stellar activity variations with high accuracy.

### $S_{MW}$ Index

We calculate the Mount Wilson  $S$  index and the  $\log_{10}(R'_{HK})$  by using the original Noyes et al. (1984) procedure, following Lovis et al. (2011) and Suárez Mascareño et al. (2015, 2017a). We define two triangular-shaped passbands with full width half maximum (FWHM) of  $1.09 \text{ Å}$  centred at  $3968.470 \text{ Å}$  and  $3933.664 \text{ Å}$  for the Ca II H&K line cores, and for the continuum we use two  $20 \text{ Å}$  wide bands centred at  $3901.070 \text{ Å}$  (V) and  $4001.070 \text{ Å}$  (R), as shown in figure 2.

Then the  $S$ -index is defined as

$$S = \alpha \frac{\tilde{N}_H + \tilde{N}_K}{\tilde{N}_R + \tilde{N}_V} + \beta, \quad (1)$$

where  $\tilde{N}_H, \tilde{N}_K, \tilde{N}_R$  and  $\tilde{N}_V$  are the mean fluxes per wavelength unit in each passband, while  $\alpha$  and  $\beta$  are calibration constants fixed as  $\alpha = 1.111$  and  $\beta = 0.0153$ . The  $S$  index ( $S_{MW}$ ) serves as a measurement of the Ca II H&K core flux normalized to the neighbour continuum. As a normalized index to compare it to other stars we compute the  $\log_{10}(R'_{HK})$  following Suárez Mascareño et al. (2015).

### $H\alpha$ Index

We also use the  $H\alpha$  index, with a simpler passband following Gomes da Silva et al. (2011) and Suárez Mascareño et al. (2017a). It consists of a rectangular bandpass with a width of  $1.6 \text{ Å}$  and centred at  $6562.808 \text{ Å}$  (core), and two continuum bands of  $10.75 \text{ Å}$  and a  $8.75 \text{ Å}$  wide centred at  $6550.87 \text{ Å}$  (L) and  $6580.31 \text{ Å}$  (R), respectively, as seen in Figure 3.

Thus, the  $H\alpha$  index is defined as

$$H\alpha_{\text{Index}} = \frac{\tilde{H}\alpha_{\text{core}}}{\tilde{H}\alpha_L + \tilde{H}\alpha_R}. \quad (2)$$

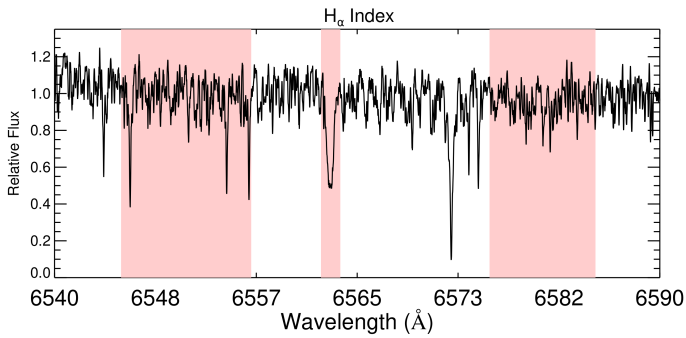


Fig. 3: Spectrum of the M-type star GJ 625 showing the  $H\alpha$  region of the spectrum. The light-red shaded regions show the filter passband and continuum bands.

Where  $\tilde{H}\alpha_{\text{core}}$ ,  $\tilde{H}\alpha_L$  and  $\tilde{H}\alpha_R$  are the mean fluxes per wavelength unit in each of the previously defined passbands.

### 3.2. Radial velocities

The radial-velocity measurement in the HARPS-N standard pipeline is determined by a Gaussian fit of the cross correlation function (CCF) of the spectrum with a synthetic stellar template (Baranne et al. 1996; Pepe et al. 2000) that consists on a series of delta functions at the positions of isolated stellar lines at wavelength longer than 4400 Å. In the case of M-dwarfs, due to the huge number of line blends, the cross correlation function is not Gaussian, resulting in a less precise Gaussian fit which might cause distortions in the radial-velocity measurements and decrease the sensibility in the measurement of the variations in the full width half maximum (FWHM) of the CCF. To deal with this issue we tried two different approaches as in Suárez Mascareño et al. (2017a).

The first one consisted in using a slightly more complex model for the CCF fitting, a Gaussian function plus a second order polynomial using only the central region of the CCF function. We use a 15 km s<sup>-1</sup> window centred at the minimum of the CCF. This configuration provides the best stability of the measurements. Along with the measurements of the radial velocity, we obtain the FWHM of the cross correlation function which we also use to track variations in the activity level of the star. A second approach to the problem was to recompute the radial velocities using the TERRA pipeline (Anglada-Escudé & Butler 2012), which is a template matching algorithm with a high signal to noise stellar spectral template. Every spectrum is corrected for both barycentric and stellar radial velocity to align it to the frame of the solar system barycenter. The radial velocities are computed by minimizing the  $\chi^2$  of the residuals between the observed spectra and shifted versions of the stellar template, with all the elements contaminated by telluric lines masked. In this case we are using the Doppler information at wavelength longer than 4550 Å. All radial-velocity measurements are corrected from the secular acceleration of the star.

For the bisector span measurement we rely on the pipeline results, as it does not depend on the fit but on the CCF itself. The bisector has been a standard activity diagnostic tool for solar type stars since more than 10 years ago. Unfortunately its behaviour in slow rotating stars is not as informative as it is for fast rotators (Saar & Donahue 1997; Bonfils et al. 2007). We report the measurements of the bisector span (BIS) for each radial-velocity

measurement, but we do not find any meaningful information in its analysis.

### 3.3. Quality Control of the Data

As the sampling rate of our data is not well suited for modelling fast events, such as flares, and their effect in the radial velocity is not well understood, we identify and reject points likely affected by flares by searching for an abnormal behaviour of the activity indicators (Reiners 2009). The process rejected 11 spectra that correspond to flare events of the star with obvious activity enhancement and line distortion. That leaves us with 140 HARPS-N spectroscopic observations taken over 3.3 years with a typical exposure of 900 s and an average signal to noise ratio of 56 at 5500 Å. All measurements and their uncertainties are reported in Table A.1.

## 4. Analysis

In order to properly understand the behaviour of the star, our first step is to analyse the different modulations present in the photometric and spectroscopic time-series.

We search for periodic variability compatible with both stellar rotation and long-term magnetic cycles. We compute the power spectrum using a Generalised Lomb Scargle Periodogram (Zechmeister & Kürster 2009) and if there is any significant periodicity we fit the detected period using sinusoidal model, or a double harmonic sinusoidal model to account for the asymmetry of some signals (Berdyugina & Järvinen 2005), with the MPFIT routine (Markwardt 2009). The model used for the preliminary analysis is chosen based on the reduced  $\chi^2$  of the fit.

The significance of the periodogram peak is evaluated using both the Cumming (2004) modification of the Horne & Baliunas (1986) formula to obtain the spectral density thresholds for a desired false alarm probability (FAP) level and bootstrap randomization (Endl et al. 2001) of the data. We finally opted for the power spectral density (PSD) levels given by the bootstrap process as those where the most conservative.

### Radial velocities

For the analysis of the radial velocities we use both the measurements given by the CCF and by the TERRA pipeline. We have 140 measurements distributed along 3.3 years. The star shows a mean RV of -12.850 Kms<sup>-1</sup>. The CCF RV measurements show an RMS of 2.56 ms<sup>-1</sup> with a typical uncertainty of 1.32 m s<sup>-1</sup> while the TERRA RV measurements show an RMS of 2.57 m s<sup>-1</sup> with a typical uncertainty of 1.24 m s<sup>-1</sup>. Figure 4 shows both time-series of RVs. Both sets show a very similar scatter with the TERRA data having slightly smaller error bars.

We find a clear dominant signal in the data, present in both series with a FAP <0.1% (although more significant in the TERRA data). The signal has a period of  $14.629 \pm 0.069$  days in the CCF series and  $14.629 \pm 0.077$  days in the TERRA series, a semi amplitude of  $1.85 \pm 0.13$  ms<sup>-1</sup> in the CCF data, and a semi amplitude of  $1.65 \pm 0.18$  ms<sup>-1</sup> in the TERRA data. Figure 5 shows the periodograms of both data series combined and Figure 6 shows the phase folded fits of both series. When analysing the residuals we see a structure of different signals between ~ 65 to ~ 100 days (see Fig. 5). Of those the most significant one is not the same in the CCF and TERRA data. The CCF data shows a  $74.7 \pm 1.9$  d signal with a semi amplitude of  $1.64 \pm 0.18$  ms<sup>-1</sup> while the TERRA data shows a  $85.9 \pm 2.8$  d signal with a semi



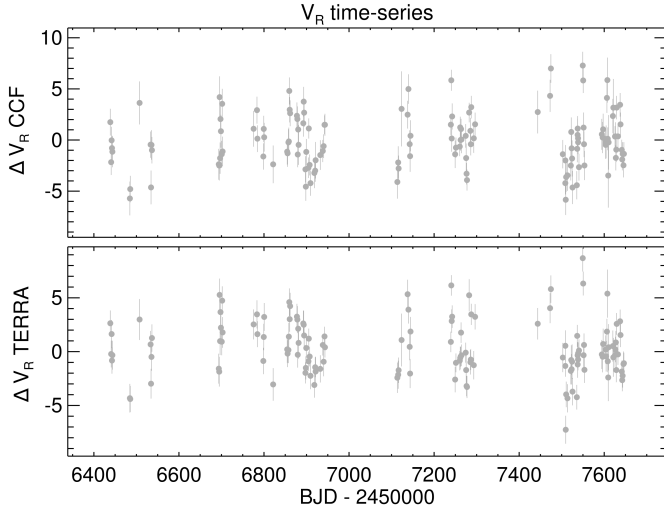


Fig. 4: Radial-velocity time series for the CCF RVs (top panel) and the TERRA RVs (bottom panel).

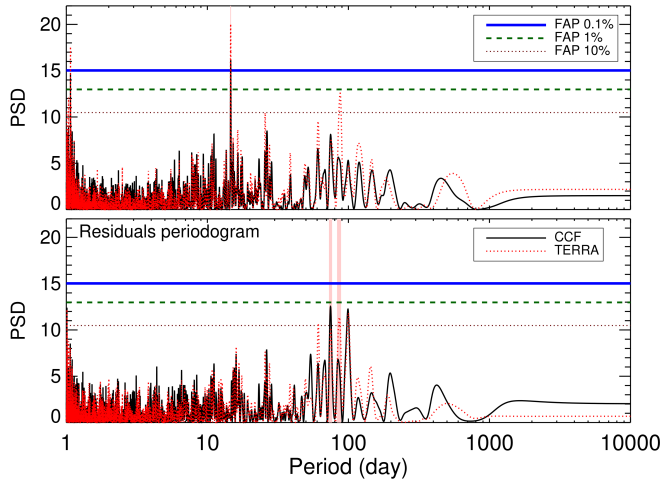


Fig. 5: Periodograms of the radial velocity time series. Top panel shows the periodogram of the raw RVs for both the CCF (black line) and TERRA (red dotted line). Bottom panel shows the periodogram of the residuals for both the CCF (black line) and TERRA (red dotted line). The light-red shaded regions show the detected periodicities.

amplitude of  $1.58 \pm 0.18 \text{ ms}^{-1}$ . Figure 7 shows the phase folded curves for those signals. No more significant signals are found in the RV data. The RMS of the remaining residuals is  $2.0 \text{ ms}^{-1}$  in both cases.

### Spectroscopic indicators

Figure 8 shows the time-series for the four spectroscopic indicators used for the activity analysis: The  $S_{MW}$  index,  $H_\alpha$  index, FWHM and bisector span time-series. For the four quantities we have 140 measurements distributed along 3.3 years. For the  $S_{MW}$  index data we measure a mean value of 0.735 (corresponding to a  $\log_{10}(R'_{HK})$  of  $-5.5$ ) with an RMS of the data of 0.094 and a typical uncertainty of the individual measurement of 0.012. Using the activity relationships of Suárez Mascareño et al. (2015, 2016) we come to expect a rotation period around  $80 \pm 20$  days. For the

Table 2: Available photometric measurements

Band	$N_{Obs}$	$T_{Span}$ (yr)	RMS (mmag)	$\sigma$ (mmag)
B	108	2.6	13.6	10.1
V	98	2.6	10.4	10.0
R	82	2.6	16.5	10.0
I	55	2.0	21.1	10.0

$H_\alpha$  index we measure a mean value of 0.41607 with an RMS of the data of 0.00729 and a typical uncertainty of 0.00070. For the case of the FWHM time series we measure a mean FWHM of  $3.83 \text{ km s}^{-1}$  with an RMS of the data of  $5.32 \text{ m s}^{-1}$  and a typical uncertainty of  $2.0 \text{ m s}^{-1}$ . For the Bisector Span we measure a mean Span of  $-6.72 \text{ m s}^{-1}$  with an RMS of the data of  $2.28 \text{ m s}^{-1}$  and a typical uncertainty of  $2.0 \text{ m s}^{-1}$ .

Figure 9 shows the periodograms for the four spectroscopic indicators. We see the sign of a long term signal in both the  $S_{MW}$  and  $H_\alpha$  indexes. In the  $S_{MW}$  index periodogram it appears as a double peak at  $\sim 1.7 \text{ yr}$  and  $\sim 3.2 \text{ yr}$ , with large uncertainties in both cases. In the  $H_\alpha$  index periodogram it appears a single peak at  $\sim 3.4 \text{ yr}$ . These signals would be compatible with short magnetic cycles, either flip-flop or global cycles (Berdyugina & Usoskin 2003; Moss 2004; Suárez Mascareño et al. 2016). The longer period peaks in both indexes seem to be the mark of the same  $\sim 3.4 \text{ yr}$  signal, while the short period peak in the  $S_{MW}$  index might be an artefact caused by the signal being extremely asymmetric. It might also be a flip-flop cycle, combined with a  $3.4 \text{ yr}$  global cycle. More observations will be needed to confirm and constrain the cycle length and nature. Our  $3.3 \text{ yr}$  baseline of observations is too short to reach a unique conclusion on the nature of these long term signals. Apart from the long term signals, three shorter period signals appear in the  $S_{MW}$ ,  $H_\alpha$  and FWHM time series of 74, 85 and 82 days respectively. Those signals are consistent with the expected rotation period of the star. The  $S_{MW}$  index signal is a  $73.7 \pm 2.2$  days signal with a semi-amplitude of  $0.0413 \pm 0.0020$  detected with a FAP  $< 1\%$ . The signal in the  $H_\alpha$  index is a  $85.2 \pm 2.2$  days signal with a semi-amplitude of  $0.00217 \pm 0.00014$  detected with a FAP  $< 10\%$ . Finally the FWHM signal has a period of  $82.0 \pm 3.1$  days and a semi-amplitude  $4.03 \pm 0.38 \text{ ms}^{-1}$ , and a FAP  $< 0.1\%$ . Figure 10 shows the phase folded curves of the three signals.

No more significant signals are found in any of the time-series after subtracting these signals.

### Photometry

In order to confirm the possible activity-induced signals present in the RV time-series and in the time-series of spectroscopic indicators we analyse the BVRI photometric time-series. Figure 11 and Table 2 show the available data. All series show the presence of some long-term evolution which is still not well covered by our observation baseline.

We subtract the long term evolution using a polynomial fit and analyse the residuals of the fit for periodic signals. Figure 12 shows the periodograms of the time series for the four filters. Several significant signals appear in the periodograms of the different time series, but we find one common periodicity for the  $m_B$ ,  $m_V$  and  $m_R$  series at  $\sim 74 \text{ d}$ . We do not find any significant signal in the  $m_I$  series periodogram. Being the I band the smallest dataset it is not surprising. We find a very significant (FAP  $< 0.1\%$ ) signal at  $73.9 \pm 3.4$  days with a semi-amplitude of  $12.1 \pm 0.3 \text{ mmag}$  in the B band time series (Fig. 13, left panel), a

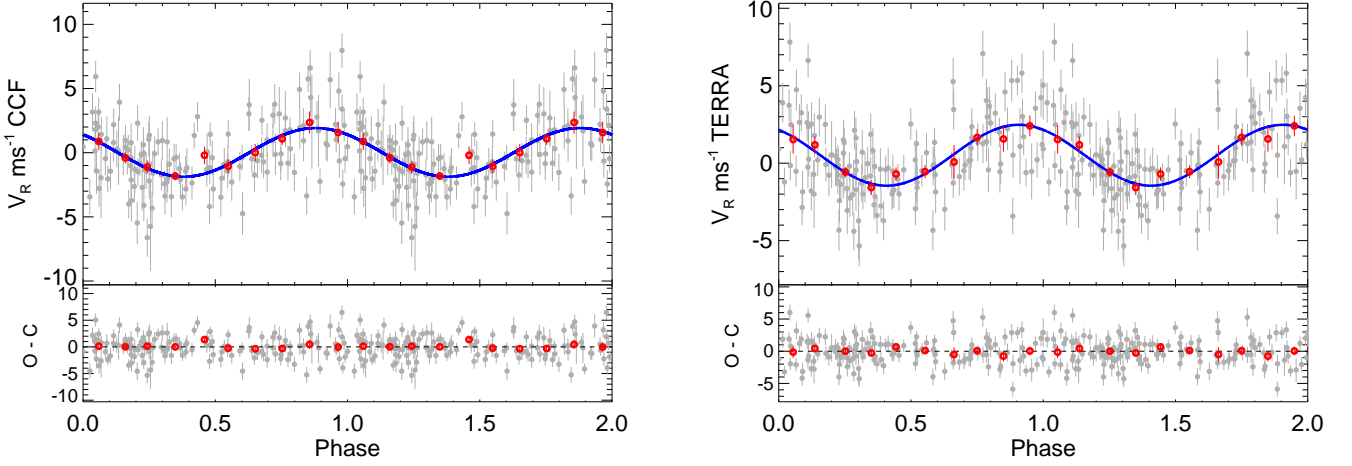


Fig. 6: Phase folded curve of the raw RV data using the 14.6 days periodicity. Left panel shows the CCF measurements, right panel the TERRA measurements. Red dots are the same points binned in phase with a bin size of 0.1. The error bar of a given bin is estimated using the weighted standard deviation of binned measurements divided by the square root of the number of measurements included in this bin. The blue solid line shows the best fit to the data using a sinusoidal fit.

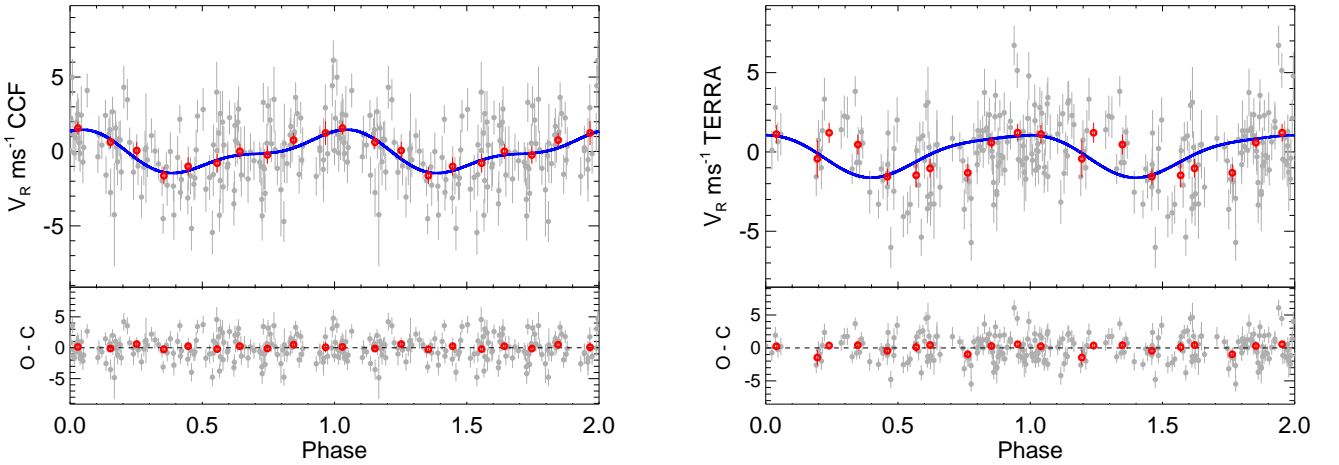


Fig. 7: Phase folded curve of the RV data using the 74 days periodicity for the CCF data (left panel) and the 86 days periodicity for the TERRA data (right panel) after subtracting the signals shown in Fig. 6. Red dots are the same points binned in phase with a bin size of 0.1. The error bar of a given bin is estimated using the weighted standard deviation of binned measurements divided by the square root of the number of measurements included in this bin. The blue solid line shows the best fit to the data using a double harmonic sinusoidal fit.

significant ( $\text{FAP} < 1\%$ ) signal at  $73.9 \pm 3.7$  days with a semi-amplitude of  $8.2 \pm 0.3$  mmag in the V band time series (Fig. 13, middle panel) and a less significant ( $\text{FAP} < 10\%$ ) signal at  $73.6 \pm 2.8$  days with a semi-amplitude of  $7.8 \pm 0.3$  mmag for the R band time series (Fig. 13, right panel). No more significant signals are found in the V and R band series after subtracting the detected signals. For the case of the B band there is a remaining signal at  $\sim 1$  yr with a second peak at  $\sim 0.5$  yr which seem to be an artefact.

## 5. Interpretation of the detected signals

The previous analysis unveiled several signals at different time-scales. Some of them are common among different datasets. Ta-

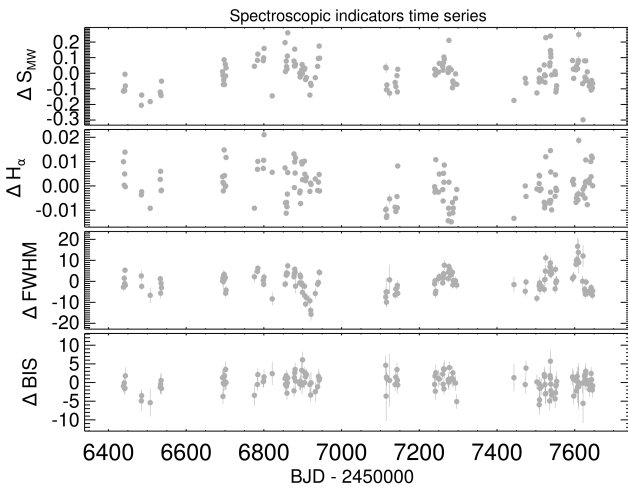
ble 3 shows the measured signals for the different datasets of GJ 625. We can identify 6 different signals: At  $\sim 3$  yr, at  $\sim 1.6$  yr, at  $\sim 85$  d, at  $\sim 82$  d, at  $\sim 74$  d and at  $\sim 14.6$  d.

The 3.4 yr signal appears as a significant peak in the  $H_\alpha$  index time-series and as a less significant one in the  $S_{MW}$  index time-series indicating a probable common origin. This signal is probably the fingerprint of the magnetic cycle of the star. A 3.4 yr cycle is short for what one could expect in solar type stars, but is in the range of previous measurements in M-dwarfs (Robertson et al. 2013; Suárez Mascareño et al. 2016). The signal at 1.7 yr could have different interpretations. On one hand, we could either be seeing the first harmonic of the 3 yr signal, because of the non-sinusoidal shape of the cycle (Waldmeier 1961; Baliunas et al. 1995). On the other hand, it could be a flip-flop cycle, i.e. a

Table 3: Detected signals in the different datasets of GJ 625. Parameters have been calculated using least squares minimization.

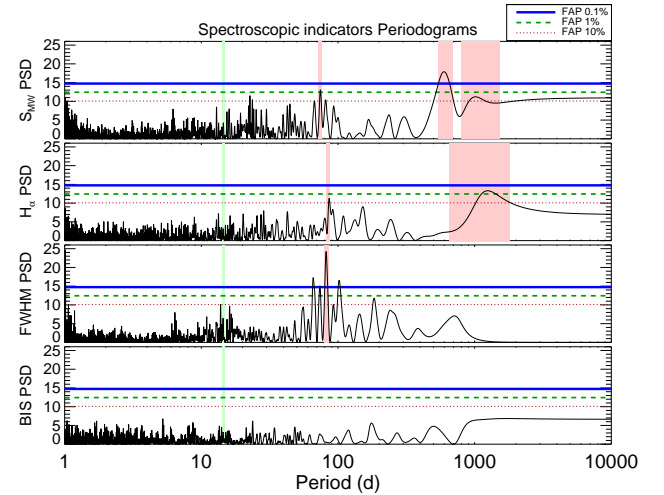
Dataset	14.6 d	Amp	74 d	Amp	82 d	Amp
RV CCF	$14.629 \pm 0.069$ d	$1.85 \pm 0.13$ ms <sup>-1</sup>	$74.7 \pm 1.9$ d	$1.64 \pm 0.18$ ms <sup>-1</sup>		
RV TERRA	$14.629 \pm 0.077$ d	$1.65 \pm 0.18$ ms <sup>-1</sup>				
$S_{MW}$			$73.7 \pm 2.2$ d	$0.0413 \pm 0.0020$		
$H_\alpha$						
FWHM					$82.0 \pm 3.1$ d	$4.03 \pm 0.38$ ms <sup>-1</sup>
$m_B$			$73.9 \pm 3.4$ d	$12.1 \pm 0.3$ mmag		
$m_V$			$73.9 \pm 3.7$ d	$8.2 \pm 0.3$ mmag		
$m_R$			$73.6 \pm 2.8$ d	$7.8 \pm 0.3$ mmag		

Dataset	85 d	Amp	1.7 yr	Amp	3.4 yr	Amp
RV CCF						
RV TERRA	$85.9 \pm 2.8$ d	$1.58 \pm 0.18$ ms <sup>-1</sup>				
$S_{MW}$			$1.7 \pm 0.2$ yr	$0.08162 \pm 0.0024$	$3.2 \pm 1.0$ yr	$0.05849 \pm 0.0024$
$H_\alpha$	$85.2 \pm 2.2$ d	$0.00217 \pm 0.00014$			$3.4 \pm 1.6$ yr	$0.00593 \pm 0.00017$
FWHM						
$m_B$						
$m_V$						
$m_R$						


Fig. 8: Time-series of the spectroscopic indicators. From top to bottom  $S_{MW}$  index,  $H_\alpha$  index, FWHM (in ms<sup>-1</sup>) and bisector span (in ms<sup>-1</sup>) time-series.

cycle of spatial rearrangement of active regions (Berdyugina & Usoskin 2003; Moss 2004). The short baseline of observations proves to be a problem to give a correct interpretation of these signals. We could be measuring the global cycle and a flip flop cycle, or the global cycle (3 yr) and its first harmonic or even a flip-flop cycle and its first harmonic. At this stage, with our baseline being as close to the measured cycle length we cannot rule out the possibility of having an artefact of a poorly constrained long term signal. Many years of data are probably needed before giving a definitive answer.

The group of signals at 74, 82 and 85 days that appear in the different spectroscopic indicators, photometric series and in the radial velocity series, are probably related to the stellar rotation. Given the activity level of the star ( $\log_{10}(R'_{HK}) = -5.5 \pm 0.2$ )


Fig. 9: Periodograms of the spectroscopic indicators. From top to bottom  $S_{MW}$  index,  $H_\alpha$  index, FWHM and bisector span time-series. The light-red shaded regions show the detected periodicities. The light green shaded region shows the position of the 14.6 d signal detected in RV.

we expect the rotation period to be around  $80 \pm 20$  days (Suárez Mascareño et al. 2015, 2016), and the semi amplitude of the induced radial velocity signal to be  $\sim 1.5$  ms<sup>-1</sup> (Suárez Mascareño et al. 2017b). Scandariato et al. (2017) found a similar periodicity using a pooled variance analysis in the Ca II H&K and  $H_\alpha$  fluxes, and the V-band photometric time series. The 5 signals around 74 days (RV, CCF,  $S_{MW}$ ,  $m_B$ ,  $m_V$  and  $m_R$ ) give us a strong indication of the stellar rotation, probably in a region close to the equator. The decline in amplitude when moving to redder bands in photometry might be an indication that we are measuring a modulation based on photospheric inhomogeneities, for which the contrast gets reduced when going to redder wavelength. The

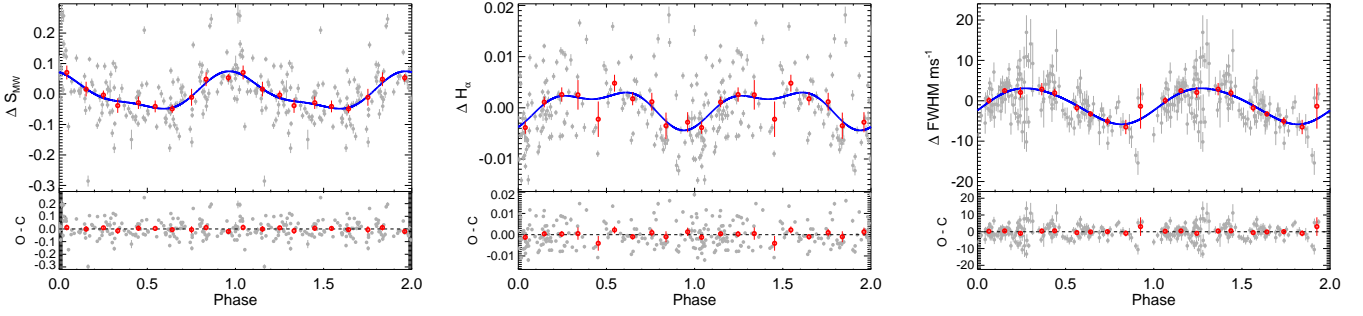


Fig. 10: Phase folded curve for the  $S_{MW}$  index time series using the 74 d period, for the detrended  $H_\alpha$  index time-series using the 85 d period, and for the FWHM time-series using the 82 d period. Grey dots are the individual measurements after subtracting the long term variations. Red dots are the same points binned in phase with a bin size of 0.1. The error bar of a given bin is estimated using the weighted standard deviation of binned measurements divided by the square root of the number of measurements included in this bin. The blue solid line shows the best fit to the data using a double harmonic sinusoidal fit.

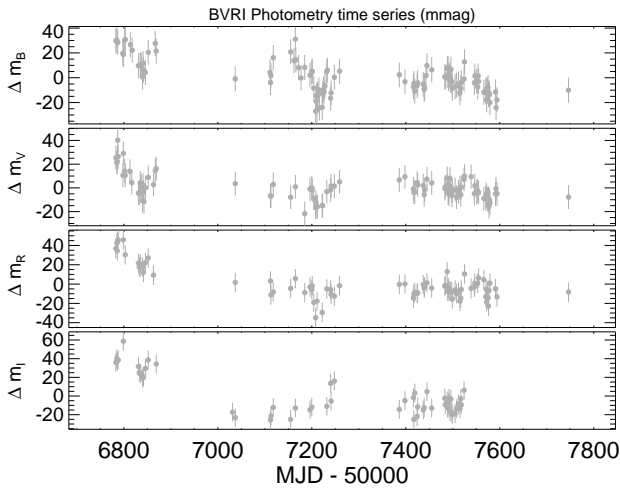


Fig. 11: Time-series of the BVRI photometry. From top to bottom  $m_B$ ,  $m_V$ ,  $m_R$  and  $m_I$  time-series.

signal at 85 days seen in the  $H_\alpha$  index and RV TERRA time series probably shows the rotation period at higher latitudes, giving us a hint on the differential rotation of this star. Being a signal only present in the  $H_\alpha$  and RV variations we are probably seeing a modulation based only on chromospheric inhomogeneities. The 82 days signal seen in the FWHM could be both a signal based on inhomogeneities in an intermediate latitude, or an average of all the measured inhomogeneities along all latitudes. The two different RV induced signals for the two algorithms could imply that the two different RV algorithms are sensitive to the effect of different groups of inhomogeneities. While the CCF measurements seems to go in line with the photometric and Ca II H&K variations, the TERRA measurements appear coherent the  $H_\alpha$  variations.

The signal at 14.6 days appears in both analyses of the RV time-series with parameters that are consistent with each other. There is no evidence of signals at this period in any of the available activity proxies (see Table 3).

As a second test we measured the Spearman correlation coefficient between the  $S_{MW}$ , the  $H_\alpha$  index, the FWHM, the bisector span and the radial velocities. We do not find a strong correlation between any of these quantities and the raw radial velocities. The

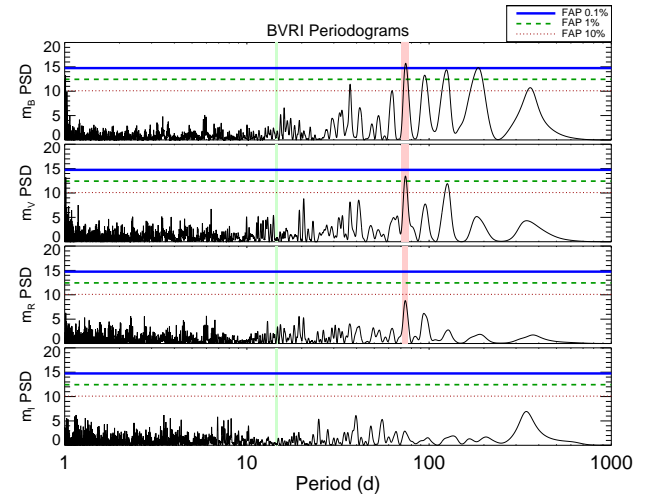


Fig. 12: Periodograms for the BVRI photometry. From top to bottom  $m_B$ ,  $m_V$ ,  $m_R$  and  $m_I$  periodograms. The light-red shaded regions show the detected periodicities. The light green shaded region shows the position of the 14.6 d signal detected in RV.

only significant one being between the FWHM and the RVs, specially with the CCF ones. All the correlation coefficients remain non significant if we subtract 74 and 85 days signals, isolating the 14.6 days signal (see Table. 4). For the case of the FWHM vs RV correlation we see the coefficient going down significantly. When we subtract the 14.6 d signal isolating the 74 d or 85 d signals we see the RV vs  $S_{MW}$  correlation coefficients going up and the RV vs FWHM correlation coefficient recovering the raw value. This constitutes a new evidence of the stellar origin of the 74 d and 85 d signals, and of the planetary origin of the 14.6 d one. Although the correlation coefficients are not very high in any case, it seems clear that isolating the 14.6 d signal reduces the correlation between the different activity proxies and the RV measurements, while isolating the 74 d or 85 d signal does not, and even increases it for the  $S_{MW}$ .

Following this idea, we subtract the linear correlation between the radial velocity and the two activity diagnostic indexes that showed a significant correlation. When doing this we see, that the strength of the 14.6 d signal remains constant, or even



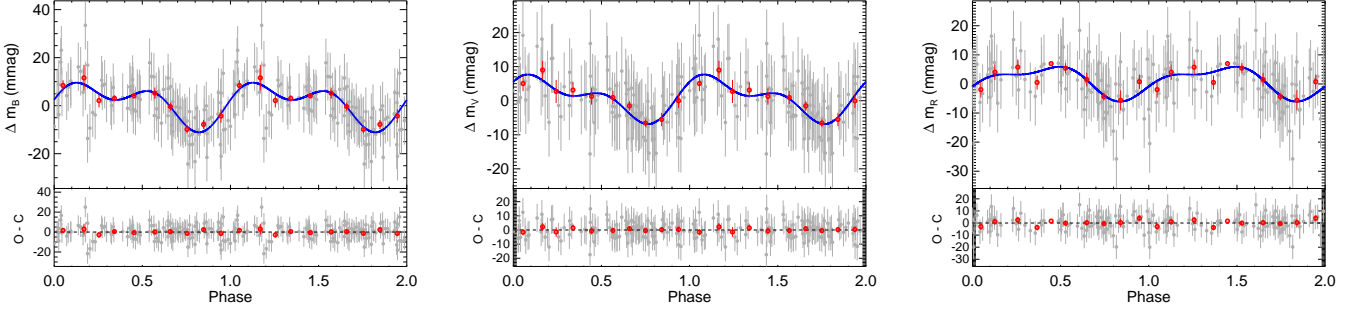


Fig. 13: Phase folded curve of the data for the B, V and R filter time series using the 74 days periodicity. Grey dots are the individual measurements after subtracting the long term variations. Red dots are the same points binned in phase with a bin size of 0.1. The error bar of a given bin is estimated using the weighted standard deviation of binned measurements divided by the square root of the number of measurements included in this bin. The blue solid line shows the best fit to the data using a double harmonic sinusoidal fit.

Table 4: Activity - Radial-velocity correlations. The parenthesis value indicates the significance of the correlation. Note: Long term variations of activity indicators have been subtracted.

Parameter	Raw data	14.6 d signal	74 d signal	85 d signal
$S_{MW}$ vs $V_R CCF$	0.08 ( $1\sigma$ )	-0.05 ( $<1\sigma$ )	0.14 ( $2\sigma$ )	
$S_{MW}$ vs $V_R TERRA$	0.09 ( $1\sigma$ )	-0.01 ( $<1\sigma$ )		0.13 ( $2\sigma$ )
$H_\alpha$ vs $V_R CCF$	-0.08 ( $1\sigma$ )	-0.08 ( $1\sigma$ )	0.02 ( $<1\sigma$ )	
$H_\alpha$ vs $V_R TERRA$	0.01 ( $<1\sigma$ )	-0.03 ( $<1\sigma$ )		0.05 ( $<1\sigma$ )
FWHM vs $V_R CCF$	0.23 ( $2\sigma$ )	0.14 ( $1\sigma$ )	0.22 ( $2\sigma$ )	
FWHM vs $V_R TERRA$	0.15 ( $2\sigma$ )	0.06 ( $<1\sigma$ )		0.14 ( $2\sigma$ )
BIS vs $V_R CCF$	0.04 ( $<1\sigma$ )	0.05 ( $<1\sigma$ )	0.06 ( $<1\sigma$ )	
BIS vs $V_R TERRA$	-0.01 ( $<1\sigma$ )	0.01 ( $<1\sigma$ )		-0.01 ( $<1\sigma$ )

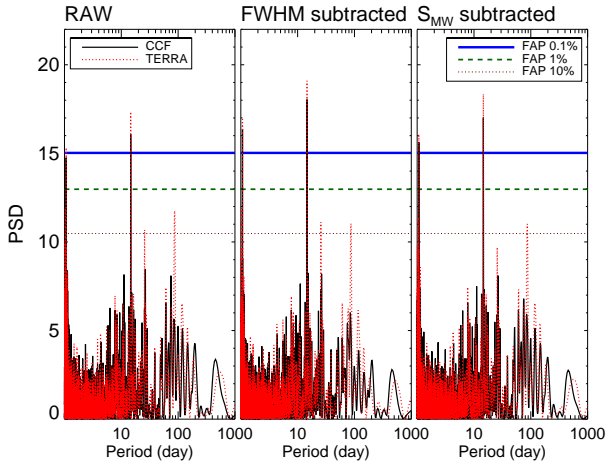


Fig. 14: Periodograms for the radial velocity after removing the correlation with the different activity diagnostic tools that showed a significant correlation coefficient. From left to right there is the periodogram for the original data, the periodogram after detrending against the FWHM, and against the  $S_{MW}$  index.

gets increased, while the significance of the 74 d and 85 d signals gets slightly reduced in all cases (see Fig. 14).

Keplerian signals are deterministic and consistent in time. When measuring one signal, it is expected to find the significance of the detection increasing steadily with the number of

observations, as well as the measured period being stable over time. However, in the case of activity related signal this is not necessarily the case. As the stellar surface is not static, and the configuration of active regions may change with time, changes in the phase of the modulation and in the detected period are expected (Affer et al. 2016; Suárez Mascareño et al. 2017a; Mortier & Collier Cameron 2017). Even the disappearance of the signal at certain seasons is possible. To study the evolution of both signals we perform a simultaneous fit of the detected periodicities in each of the time series, and then use the derived parameters to subtract the contribution of one of them leaving the other "isolated". We then perform the stacked periodograms using a very narrow frequency window around each of the signals. Fig. 15 shows the evolution of the PSD of the detection of both isolated signals. Once we gain enough signal to noise, the 14.6 d signal increases steadily with the number of measurements. On the other hand the behaviour of the 74 d and 85 d signals is more erratic, especially for the case of the 85 days signal in the TERRA data. This is consistent with the attributed stellar origin, although we cannot rule out that the fluctuations are created by the lack of a sufficient signal to noise ratio for those signals.

Of the different significant radial-velocity signals detected in our data, it seems clear that the one at 14.6 d has a planetary origin, while the signals at 74 d and 85 d have stellar activity origin.

Finally, an analysis of the spectral window ruled out that the peak in the periodogram attributed to the keplerian signal is an artefact of the time sampling. No features appear at 14.6 d days even after masking the oversaturated regions of the power spectrum. The region around 70-90 days is more complicated in the



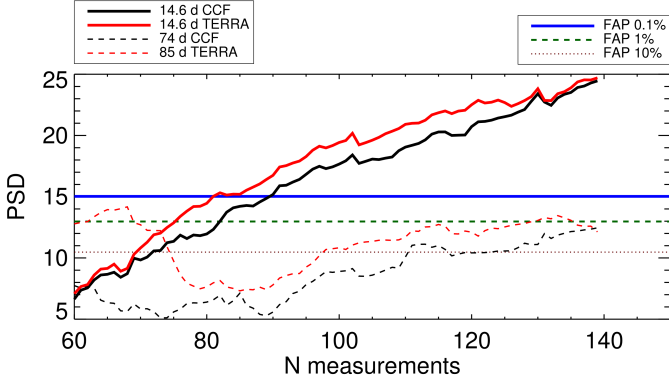


Fig. 15: Evolution of the significance of the detections for the isolated signals. Thick lines show the 14.6 days signal, dashed lines represent the 74 d and 85 d signals. Black lines represent the CCF signals, red lines show the TERRA signals.

HARPS-N spectral window, casting some doubts on those periodicities, but that region is perfectly clean in the spectral window for the photometric time series. That suggests that the signals that we attributed to rotation in the RVs and spectroscopic indicators are real, but it also might explain the differences between the various indicators and the two different RV time series through spectral leakage of the real signal (Scargle 1982). We also recognize a prominent feature at 36.8 days, which should be treated with caution when searching for additional planets in the future. Figure 16 shows the spectral windows of the HARPS-N and photometric time series, along with a comparison between the RV periodogram around the 14.6 d signal and the spectral window in the same region. Following Rajpaul et al. (2016), we tried to re-create the 14.6 days signal by injecting the  $P_{\text{Rot}}$  signal along with a second signal at  $P_{\text{Rot}}/2$  at 1000 randomized phase shifts with a white noise model. Additionally we added a second set of signals at 3 yr and 1.5 yr to account for the possible effect of the magnetic cycle. We were never able to generate a signal at 14.6 days, or any significant signal at periods close to 14.6 days. It seems very unlikely that any of the signals are artefacts of the sampling. The process on the other hand created many spurious peaks at periods between 35 and 120 days. Future observations should take into account the possibility of having aliases and artefacts of the rotation arising in a wide range of periodicities.

## 6. MCMC modelling of the GJ 625 b planet

The analysis of the radial-velocity time series and of the activity indicators leads us to conclude that the best explanation of the observed data is the existence of a planet orbiting the star GJ 625 at the period of 14.6 d. The best solution comes from a super-Earth with a minimum mass of  $2.8 M_{\oplus}$  orbiting at 0.078 AU of its star.

In order to quantify the uncertainties of the orbital parameters of the planet, we perform a bayesian analysis using the code ExoFrr (Balan & Lahav 2009) as outlined in Suárez Mascareño et al. (2017a). This code follows the Bayesian method described in Gregory (2005); Ford (2005); Ford & Gregory (2007). A single planet can be modelled using the following formula:

$$v_i = \gamma - K[\sin(\theta(t_i + \chi P) + \omega) + e \sin \omega] \quad (3)$$

where  $\gamma$  is system radial velocity;  $K$  is the velocity semi-amplitude equal to  $2\pi P^{-1}(1 - e^2)^{-1/2}a \sin i$ ;  $P$  is the orbital pe-

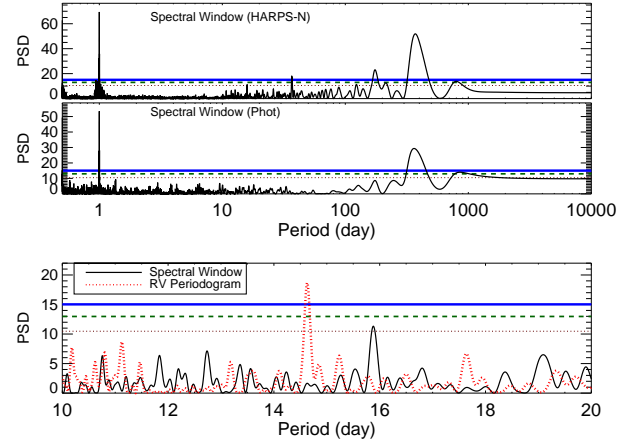


Fig. 16: Spectral windows for the HARPS data (top panel) and the photometric data (mid panel). Bottom panel shows the RV periodogram (red dotted line) compared to the spectral window (black solid line) in the range of periods around the signal for the planet candidate.

riod;  $a$  is the semi-major axis of the orbit;  $e$  is the orbital eccentricity;  $i$  is the inclination of the orbit;  $\omega$  is the longitude of periastron;  $\chi$  is the fraction of an orbit, prior to the start of data taking, at which periastron occurs (thus,  $\chi P$  equals the number of days prior to  $t_i = 0$  that the star was at periastron, for an orbital period of  $P$  days); and  $\theta(t_i + \chi P)$  is the angle of the star in its orbit relative to periastron at time  $t_i$ , also called the true anomaly.

To fit the previous equation to the data we need to specify the six model parameters,  $P$ ,  $K$ ,  $\gamma$ ,  $e$ ,  $\omega$  and  $\chi$ . Observed radial-velocity data,  $d_i$ , can be modelled by the equation:  $d_i = v_i + \epsilon_i + \delta$  (Gregory 2005), where  $v_i$  is the calculated radial velocity of the star and  $\epsilon_i$  is the uncertainty component arising from accountable but unequal measurement error which are assumed to be normally distributed. The term  $\delta$  contains any unknown measurement error. Any noise component that cannot be modelled is described by the term  $\delta$ . The probability distribution of  $\delta$  is chosen to be a Gaussian distribution with finite variance  $s^2$ . Therefore, the combination of uncertainties  $\epsilon_i + \delta$  has a Gaussian distribution with a variance equal to  $\sigma_i^2 + s^2$  (see Balan & Lahav 2009, for more details).

In Table 5 we show the final parameters and uncertainties obtained with the MCMC bayesian analysis with the code ExoFrr. We performed a simultaneous fit of the planetary signal and the activity induced signal using both the CCF and the TERRA data. The obtained parameters are compatible in both datasets, except for  $\omega$  and  $\chi$ . However in those cases the uncertainties are large, suggesting that more data might be needed to better define the solution. Fig. 17 and 18 show the probability densities for all the parameters in both situations and Fig. 19 shows the best fit to the data obtained for the RV signal attributed to the planet candidate GJ 625 b. The TERRA data gives a smaller RV amplitude and smaller mass and a smaller RMS of the residuals. The noise factor in both cases exceeds the typical uncertainties of our data, indicating the presence of unaccounted signals in the radial velocity data. The smaller RMS of the residuals after the fit of the TERRA data – despite showing a higher RV noise factor – and the tighter parameter results lead us to favour the model given by the TERRA data. The RMS of the remaining residuals is 1.8

$\text{m s}^{-1}$ , smaller than the HADES noise contribution estimated in Perger et al. (2017a).

## 7. Discussion

We detect the presence of a planet with a semi-amplitude of  $1.6 \text{ m s}^{-1}$  that, given the stellar mass of  $0.3 M_{\odot}$ , converts to  $m_p \sin i$  of  $2.75 M_{\oplus}$ , orbiting with a period of 14.6 d around GJ 625, an M2-type star with a mean rotation period of around 78 d and an additional activity signal compatible with an activity cycle of around 3 yr. We have seen hints of differential rotation, with the difference between the shortest and the longest period going up to 11 days.

The planet is a small super-Earth at the edge of the habitable zone of its star. Using a basic estimation of the equilibrium temperature, and a correction using the greenhouse calculated to estimate the surface temperature, we estimate a mean surface temperature of 350 K for a Bond albedo  $A = 0.3$  and Earth-like greenhouse effect. Surface temperatures close to earth surface temperature can be reached for many combinations of albedo and greenhouse effect. Following Kasting et al. (1993) and Selsis et al. (2007), we perform a simple estimation of the habitable zone (HZ) of this star. The HZ would go from 0.099 to 0.222 AU in the narrowest case (cloud free model), and 0.057 to 0.305 AU in the broader one (fully clouded model). Figure 20 shows the distribution of surface mean temperatures for the different combination of bond albedo and green house levels and the evolution of the habitable zone following Selsis et al. (2007). The estimation of the habitable zone performed by Kopparapu (2013) for a cloud-free model would leave the most optimistic inner limit of the HZ at 0.088 AU. If we assume that the HZ evolves with the cloud coverage of the atmosphere of the planet in the same way as in Selsis et al. (2007), then the most optimistic limit of the inner HZ would move down to 0.043 AU for a completely covered atmosphere, following almost exactly the same pattern as in Selsis et al. (2007). We find that GJ 625 b might potentially host liquid water depending on its atmospheric conditions.

The habitability of planets in close orbits around low-mass stars is nowadays a subject of debate. Planets are probably tidally locked, and exposed to the strong magnetic field, flares and UV and X-ray irradiation of their parent stars. But even if those are strong arguments against their habitability, none of them is a definitive one. Depending on the planet composition and its own magnetic field it could be able to prevent all but a small atmospheric loss (Vidotto et al. 2013; Zuluaga et al. 2013; Anglada-Escudé et al. 2016; Ribas et al. 2016; Bolmont et al. 2017).

GJ 625 b is in the lower part of the Mass vs Period diagram of known planets around M-dwarf stars with measured dynamic masses (Fig. 21). The proposed projected mass would make it the lightest planet found around an M2 star to date. Of all the known planets around M-dwarfs with dynamical masses determined  $\sim 52\%$  are super-Earths or Earth-like planets ( $< 10 M_{\oplus}$ ) at periods shorter than 100 days. Fig. 21 points out once more the lack of massive planets in close orbits around M-dwarfs, only  $\sim 9\%$  of detected planets at periods shorter than 10 days being heavier than  $10 M_{\oplus}$ , with only one going over  $1 M_{Jup}$ , as expected by the core-accretion formation model (Laughlin et al. 2004). There is also a lack of small planets ( $< 3 M_{\oplus}$ ) in close orbits ( $< 10$  days) around early M-dwarfs (M0-M2), with GJ 3998 being the only one. At periods longer than 10 days on the other hand there is a great abundance of this kind of planets.

The presence of one or more extra planets around the star GJ 625 cannot yet be ruled out at longer orbital periods and small RV amplitudes ( $< 1.5 \text{ m s}^{-1}$  for periods shorter than 3 years),

but finding them will not be easy. The rotation period, combined with the signs of differential rotation, would make difficult the detection of low amplitude planetary signals in the range of periods from 35 to 120 days, as stated at the end of Section 5. Also considering the detected magnetic cycle it would be expected to find a RV signal at 1.5 yr or 3 yr eventually arising. The most promising candidates to continue searching would be very small mass planets at very close orbits, and small mass planets in the habitable zone of the star, at periods shorter than 30 days.

The activity induced RV variations measured both using the CCF fitting and the TERRA pipeline are not consistent with each other. With the CCF fitting favouring a signal at 74 days, very similar to the ones measured in the B-, V- and R-band photometry and in the Ca II H&K variations, while the TERRA pipeline favours a 85 d signal closest to the signal measured in the  $H_{\alpha}$  index. Stellar induced signals are usually more complicated than planetary signals, and the long period and low amplitude of the signals ( $\sim 1.6 \text{ m s}^{-1}$ ), combined with their non-sinusoidal shape, could easily lead to an incorrect modelling. The spectral window of the observation series might also be playing a part here. The region around 70-100 days is a complicated one, so it cannot be ruled out that it is affecting the 82 and 85 days measurements. If we assume that this is not the case, it could be that the change in the source of RV information (a selection of lines in the CCF vs the full spectrum in TERRA) is making the two algorithms sensitive to different active regions or even different depths of the stellar atmosphere. If this were the case the use of both algorithms for the same star could prove a very useful tool for the diagnosis of activity induced signals, maybe even for the case of earlier spectral types (G and K-type stars). Further investigation using data from different stars would be needed.

GJ 625 has an estimated mass of  $0.3 M_{\odot}$ , placing it close to the theoretical limit at which a star becomes fully convective. If the proposed 3 yr magnetic cycle could be confirmed it would place GJ 625 in the small group of very small mass stars which exhibit activity cycles despite theoretical predictions suggesting they should not (Chabrier & Küker 2006; Robertson et al. 2014; Suárez Mascareño et al. 2016; Wargelin et al. 2017). The growing number of detected cycles in stars that are expected to be fully-convective, and therefore to not have a tachocline, supports the idea that the stellar dynamo might not be confined to the tachocline but instead distributed across the convection zone (Wright et al. 2016).

## 8. Conclusions

We have analysed 151 high resolution spectra along with photometric observations in 4 different bands to study the presence of planetary companions around the M-dwarf star GJ 625 and its stellar activity. For the study of this system, we extracted the radial velocity information in two different ways, on one hand using the cross correlation of the spectra with a numerical template, on the other hand by template matching the individual spectra with a high S/N template.

We detected one significant radial-velocity signals, at a period of 14.6 d. A second one arises at 74-85 days, with different periods for the different algorithms. From the available photometric and spectroscopic information we conclude that the 14.6 d signal is caused by a planet with a minimum mass of  $2.82 M_{\oplus}$  in an orbit with a semi-major axis of 0.078 AU. The planet is on the inner edge of the habitable zone, with its mean surface temperature very dependent on the atmospheric parameters. The short period of the planet makes it a potential transiting candidate. Following Winn (2010) we find the transit probability of GJ

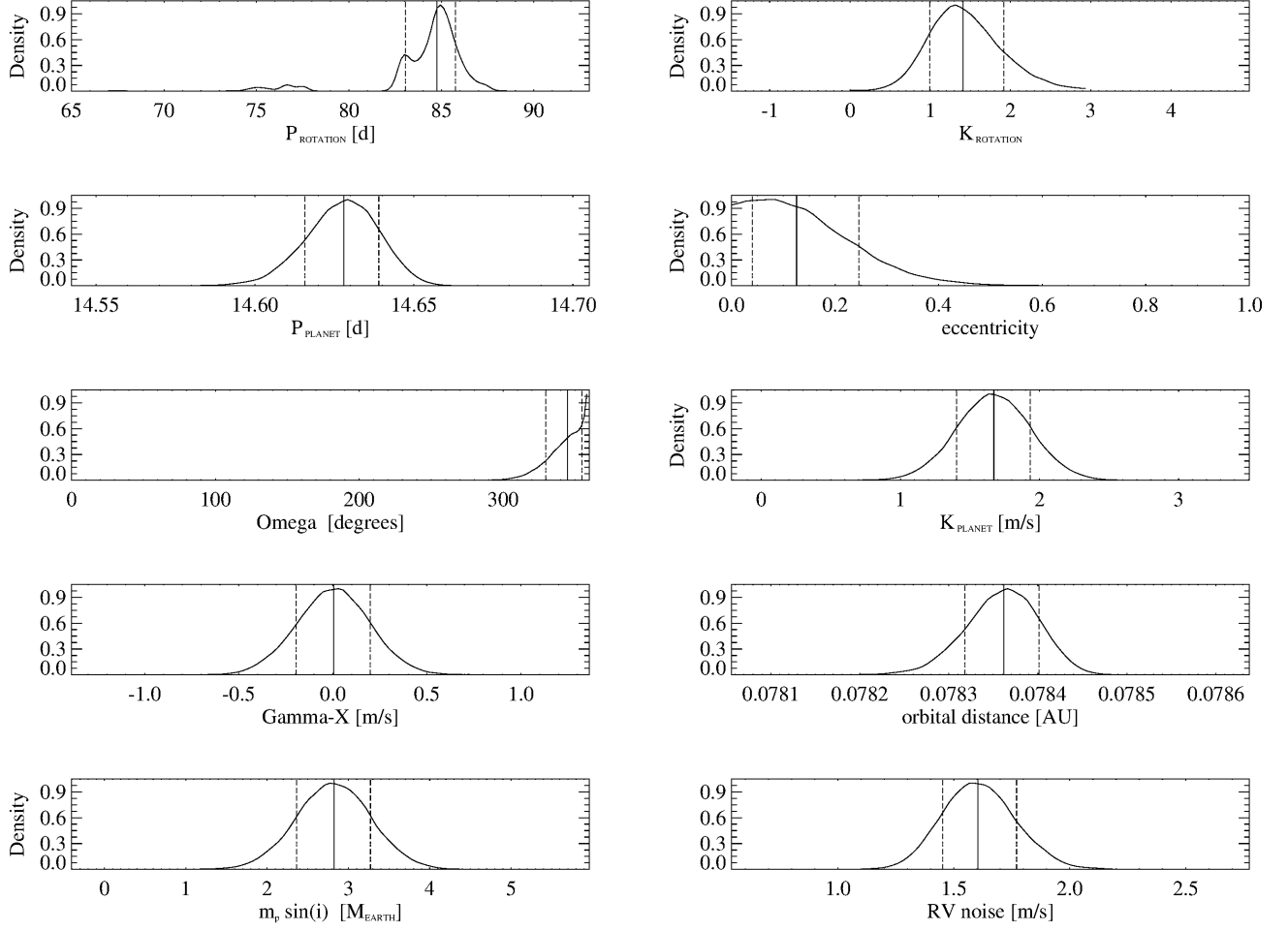


Fig. 17: Posterior distribution of model parameters of the planet companion of the M dwarf star GJ 625 using the RV measurements given by the TERRA pipeline. Vertical dashed line show the median value of the distribution and the dotted lines the  $1-\sigma$  values.

Table 5: MCMC parameters and uncertainties

Parameter	TERRA			CCF			Prior
	Value	Upper error	Lower error	Value	Upper error	Lower error	
$P_{\text{planet}}$ [d]	14.628	+0.012	-0.013	14.638	+0.012	-0.013	10.5 - 18.5
$\gamma$ [ $\text{ms}^{-1}$ + 12850]	-0.11	+0.18	-0.18	-0.07	+0.19	-0.20	-3.0 - +3.0
$e$	0.13	+0.12	-0.09	0.13	+0.13	-0.09	0.0 - 0.99
$\omega$ [deg]	343.1	+9.6	-14.8	240	+70	-180	0.0 - 360.0
$\chi$	0.94+	+0.026	-0.043	0.26	+0.45	-0.18	0.0 - 0.99
$K_{\text{planet}}$ [ $\text{ms}^{-1}$ ]	1.67	+0.29	-0.29	1.79	+0.29	-0.30	0.0 - 3.0
$a$ [AU]	0.078361	+0.000044	-0.000046	0.078399	+0.000042	-0.000045	-
$m_p \sin i$ [ $M_{\text{Earth}}$ ]	2.82	+0.51	-0.51	3.02	+0.49	-0.50	-
$P_{\text{Rot}}$ [d]	84.7	+1.3	-1.8	76.1	+8.9	-3.0	65.0 - 95.0
$K_{\text{Rot}}$ [ $\text{ms}^{-1}$ ]	1.41	+0.53	-0.47	1.25	+0.52	-0.39	0.0 - 3.0
RV noise [ $\text{ms}^{-1}$ ]	1.61	+0.18	-0.18	1.48	+0.18	-0.17	0.0 - 3.0

625 b in the range of 1.5 - 2.5 %. Detecting the transits would give a new constraining point to the mass-radius diagram and provide further opportunity for atmospheric characterization.

The second radial-velocity signal of period 74-85 d and semi amplitude of  $1.6 \text{ ms}^{-1}$  is a magnetic activity induced signal related to the rotation of the star. Using the photometric light

curves and the time-series of spectral indicators we conclude that the rotation period of the star is  $\sim 74$  days, with evidence of differential rotation up to  $\sim 85$  days. We have seen that the measured rotation period and the amplitude of the rotation induced signal match the expected results of Suárez Mascareño et al. (2015, 2016, 2017b). We also found evidence for a mag-

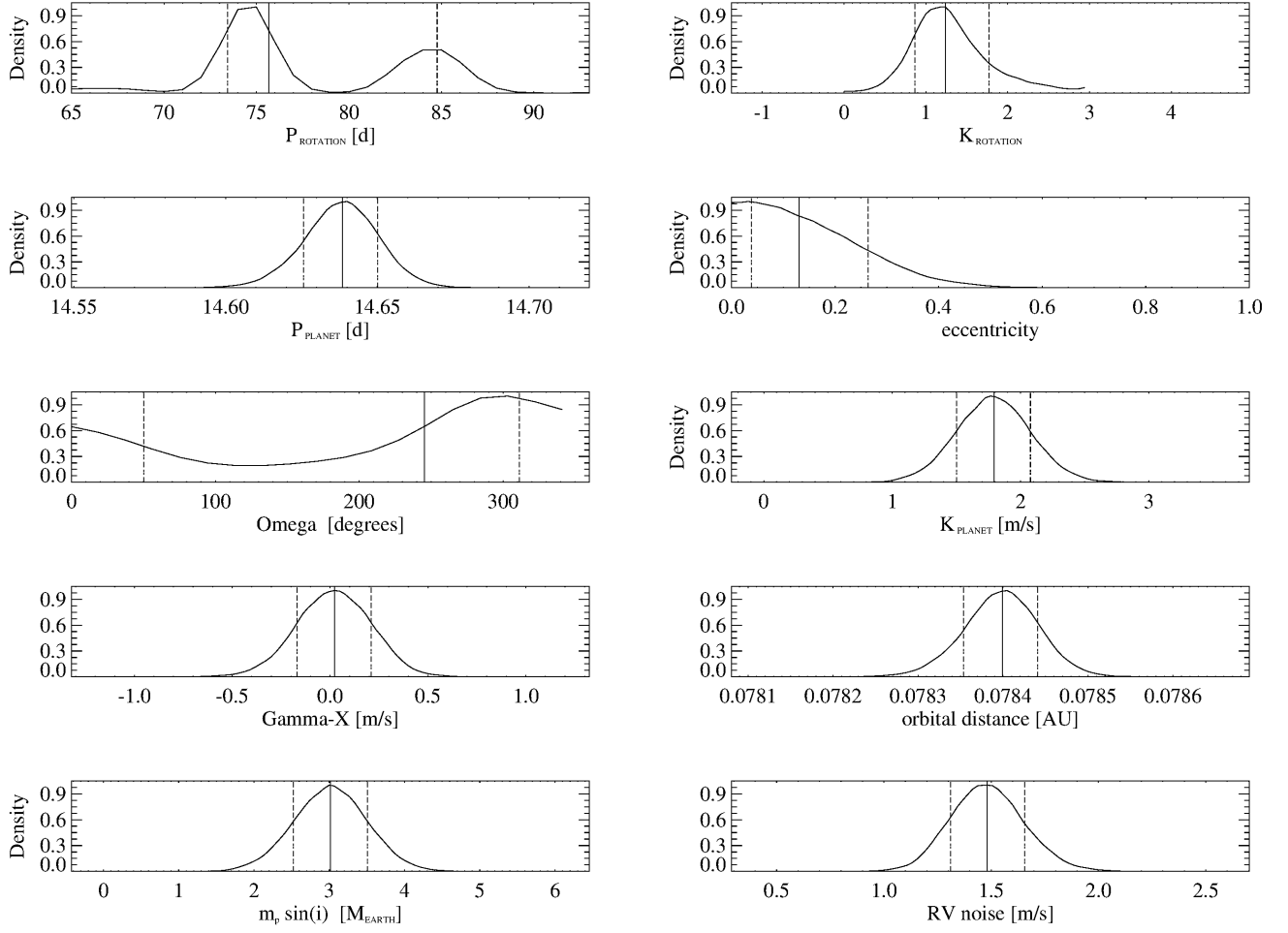


Fig. 18: Posterior distribution of model parameters of the planet companion of the M dwarf star GJ 625 using the RV measurements given by the CCFs. Vertical dashed line show the median value of the distribution and the dotted lines the  $1\text{-}\sigma$  values.

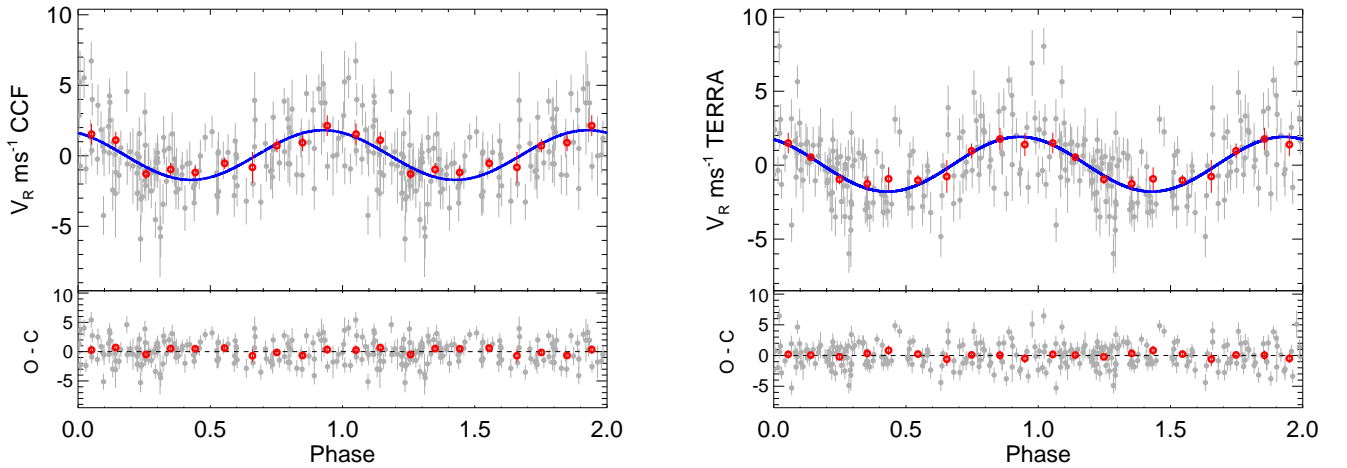


Fig. 19: Phase folded curve of the planetary signal detected in GJ 625 using the parameters of the MCMC model. Left panel shows the CCF measurements, right panel the TERRA measurements. Grey dots show the measurements after subtracting the detected activity induced signals. Red dots are the same points binned in phase with a bin size of 0.1. The error bar of a given bin is estimated using the weighted standard deviation of binned measurements divided by the square root of the number of measurements included in this bin. Blue line shows the best fit to the data using a Keplerian model.

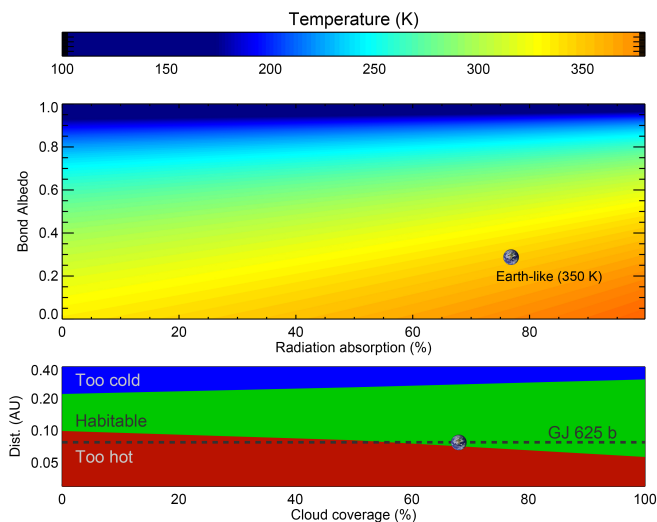


Fig. 20: Mean surface temperature of GJ 625 b as a function of albedo and the fraction of radiation absorbed by the atmosphere (top panel) and change of the habitable zone as a function of cloud coverage of the planet (bottom panel). The Earth symbol shows where it would be with an Earth-like albedo and greenhouse effect (top panel), and with an Earth-like cloud coverage (bottom panel).

netic cycle of  $\sim 3$  yr which would need future observations to be better constrained.

## Acknowledgements

We thank Guillem Anglada-Escudé for distributing the latest version of the TERRA pipeline. This research has made extensive use of the SIMBAD database, operated at CDS, Strasbourg, France and NASA's Astrophysics Data System. This work has been financed by the Spanish Ministry project MINECO AYA2014-56359-P. J.I.G.H. acknowledges financial support from the Spanish MINECO under the 2013 Ramón y Cajal program MINECO RYC-2013-14875. A.S.M acknowledges financial support from the Swiss National Science Foundation (SNSF). M. P., I. R., J.C.M., E.H., A. R., and M.L. acknowledge support from the Spanish Ministry of Economy and Competitiveness (MINECO) and the Fondo Europeo de Desarrollo Regional (FEDER) through grant ESP2016-80435-C2-1-R. mGAPS acknowledges support from INAF through the "Progetti Premiali" funding scheme of the Italian Ministry of Education, University, and Research and through the PREMIALE WOW 2013 research project. L. A. and G. M. acknowledge support from the Ariel ASI-INAF agreement N. 2015-038-R.0. The research leading to these results has received funding from the European Union Seventh Framework Programme (FP7/ 2007-2013) under Grant Agreement No. 313014 (ETA-EARTH). G.S. acknowledges financial support from "Accordo ASI-INAF" n. 2013-016-R.0 July 9, 2013.

## References

Affer, L., Micela, G., Damasso, M., et al. 2016, *A&A*, 593, A117  
 Anglada-Escudé, G., Amado, P. J., Barnes, J., et al. 2016, *Nature*, 536, 437  
 Anglada-Escudé, G. & Butler, R. P. 2012, *ApJS*, 200, 15  
 Astudillo-Defru, N., Bonfils, X., Delfosse, X., et al. 2015, *A&A*, 575, A119  
 Astudillo-Defru, N., Forveille, T., Bonfils, X., et al. 2017, *ArXiv e-prints* [arXiv:1703.05386]

Balan, S. T. & Lahav, O. 2009, *MNRAS*, 394, 1936  
 Baliunas, S. L., Donahue, R. A., Soon, W. H., et al. 1995, *ApJ*, 438, 269  
 Baranne, A., Queloz, D., Mayor, M., et al. 1996, *A&AS*, 119, 373  
 Berdyugina, S. V. & Järvinen, S. P. 2005, *Astronomische Nachrichten*, 326, 283  
 Berdyugina, S. V. & Usoskin, I. G. 2003, *A&A*, 405, 1121  
 Berta-Thompson, Z. K., Irwin, J., Charbonneau, D., et al. 2015a, *Nature*, 527, 204  
 Berta-Thompson, Z. K., Irwin, J., Charbonneau, D., et al. 2015b, *NAT*, 527, 204  
 Boisse, I., Bouchy, F., Hébrard, G., et al. 2011, *A&A*, 528, A4  
 Bolmont, E., Selsis, F., Owen, J. E., et al. 2017, *MNRAS*, 464, 3728  
 Bonfils, X., Delfosse, X., Udry, S., et al. 2013, *A&A*, 549, A109  
 Bonfils, X., Mayor, M., Delfosse, X., et al. 2007, *A&A*, 474, 293  
 Chabrier, G. & Küker, M. 2006, *A&A*, 446, 1027  
 Cosentino, R., Lovis, C., Pepe, F., et al. 2012, in *SPIE*, Vol. 8446, *Ground-based and Airborne Instrumentation for Astronomy IV*, 84461V  
 Covino, E., Esposito, M., Barbieri, M., et al. 2013, *A&A*, 554, A28  
 Cumming, A. 2004, *MNRAS*, 354, 1165  
 Delfosse, X., Bonfils, X., Forveille, T., et al. 2013, *A&A*, 553, A8  
 Dressing, C. D. & Charbonneau, D. 2013, *ApJ*, 767, 95  
 Dressing, C. D., Charbonneau, D., & Newton, E. R. 2015, in *AAS/Division for Extreme Solar Systems Abstracts*, Vol. 3, *AAS/Division for Extreme Solar Systems Abstracts*, 501.03  
 Endl, M., Cochran, W. D., Kürster, M., et al. 2006, *ApJ*, 649, 436  
 Endl, M., Kürster, M., Els, S., Hatzes, A. P., & Cochran, W. D. 2001, *A&A*, 374, 675  
 Ford, E. B. 2005, *AJ*, 129, 1706  
 Ford, E. B. & Gregory, P. C. 2007, in *Astronomical Society of the Pacific Conference Series*, Vol. 371, *Statistical Challenges in Modern Astronomy IV*, ed. G. J. Babu & E. D. Feigelson, 189  
 Gaia Collaboration, Brown, A. G. A., Vallenari, A., et al. 2016, *A&A*, 595, A2  
 Gaidos, E. 2013, *ApJ*, 770, 90  
 Gillon, M., Triaud, A. H. M. J., Demory, B.-O., et al. 2017, *Nature*, 542, 456  
 Gomes da Silva, J., Santos, N. C., Bonfils, X., et al. 2011, *A&A*, 534, A30  
 Gregory, P. C. 2005, *ApJ*, 631, 1198  
 Høg, E., Fabricius, C., Makarov, V. V., et al. 2000, *A&A*, 355, L27  
 Horne, J. H. & Baliunas, S. L. 1986, *ApJ*, 302, 757  
 Howard, A. W., Johnson, J. A., Marcy, G. W., et al. 2009, *ApJ*, 696, 75  
 Howard, A. W., Marcy, G. W., Bryson, S. T., et al. 2012, *ApJS*, 201, 15  
 Howard, A. W., Marcy, G. W., Fischer, D. A., et al. 2014, *ApJ*, 794, 51  
 Irwin, J., Berta-Thompson, Z. K., Charbonneau, D., Dittmann, J., & Newton, E. R. 2015, in *American Astronomical Society Meeting Abstracts*, Vol. 225, *American Astronomical Society Meeting Abstracts*, 258.01  
 Jehin, E., Gillon, M., Lederer, S. M., et al. 2016, in *AAS/Division for Planetary Sciences Meeting Abstracts*, Vol. 48, *AAS/Division for Planetary Sciences Meeting Abstracts*, 302.07  
 Kastings, J. F., Whitmire, D. P., & Reynolds, R. T. 1993, *ICARUS*, 101, 108  
 Kopparapu, R. K. 2013, *ApJ*, 767, L8  
 Labadie, L., Rebolo, R., Villó, I., et al. 2011, *A&A*, 526, A144  
 Laughlin, G., Bodenheimer, P., & Adams, F. C. 2004, *ApJ*, 612, L73  
 Lovis, C., Dumusque, X., Santos, N. C., et al. 2011, *ArXiv e-prints* [arXiv:1107.5325]  
 Maldonado, J., Scandariato, G., Stelzer, B., et al. 2017, *A&A*, 598, A27  
 Markwardt, C. B. 2009, in *Astronomical Society of the Pacific Conference Series*, Vol. 411, *Astronomical Data Analysis Software and Systems XVIII*, ed. D. A. Bohlender, D. Durand, & P. Dowler, 251  
 Mayor, M., Bonfils, X., Forveille, T., et al. 2009, *A&A*, 507, 487  
 Mayor, M., Marmier, M., Lovis, C., et al. 2011, *ArXiv e-prints* [arXiv:1109.2497]  
 Montet, B. T., Crepp, J. R., Johnson, J. A., Howard, A. W., & Marcy, G. W. 2014, *ApJ*, 781, 28  
 Mortier, A. & Collier Cameron, A. 2017, *ArXiv e-prints* [arXiv:1702.03885]  
 Moss, D. 2004, *MNRAS*, 352, L17  
 Newton, E. R., Irwin, J., Charbonneau, D., Berta-Thompson, Z. K., & Dittmann, J. A. 2016, *ApJL*, 821, L19  
 Noyes, R. W., Hartmann, L. W., Baliunas, S. L., Duncan, D. K., & Vaughan, A. H. 1984, *ApJ*, 279, 763  
 Oscoz, A., Rebolo, R., López, R., et al. 2008, in *Proc. SPIE*, Vol. 7014, *Ground-based and Airborne Instrumentation for Astronomy II*, 701447  
 Pepe, F., Mayor, M., Delabre, B., et al. 2000, in *SPIE*, Vol. 4008, *Optical and IR Telescope Instrumentation and Detectors*, ed. M. Iye & A. F. Moorwood, 582–592  
 Perger, M., García-Piquer, A., Ribas, I., et al. 2017a, *A&A*, 598, A26  
 Perger, M., Ribas, I., Affer, L., & Suárez-Mascares, A. 2017b, *A&A*  
 Poretti, E., Boccato, C., Claudi, R., et al. 2016, *Mem. Soc. Astron. Italiana*, 87, 141  
 Queloz, D., Henry, G. W., Sivan, J. P., et al. 2001, *A&A*, 379, 279  
 Quirrenbach, A., Amado, P. J., Seifert, W., et al. 2012, in *Proc. SPIE*, Vol. 8446, *Ground-based and Airborne Instrumentation for Astronomy IV*, 84460R  
 Rajpaul, V., Aigrain, S., & Roberts, S. 2016, *MNRAS*, 456, L6  
 Reiners, A. 2009, *A&A*, 498, 853



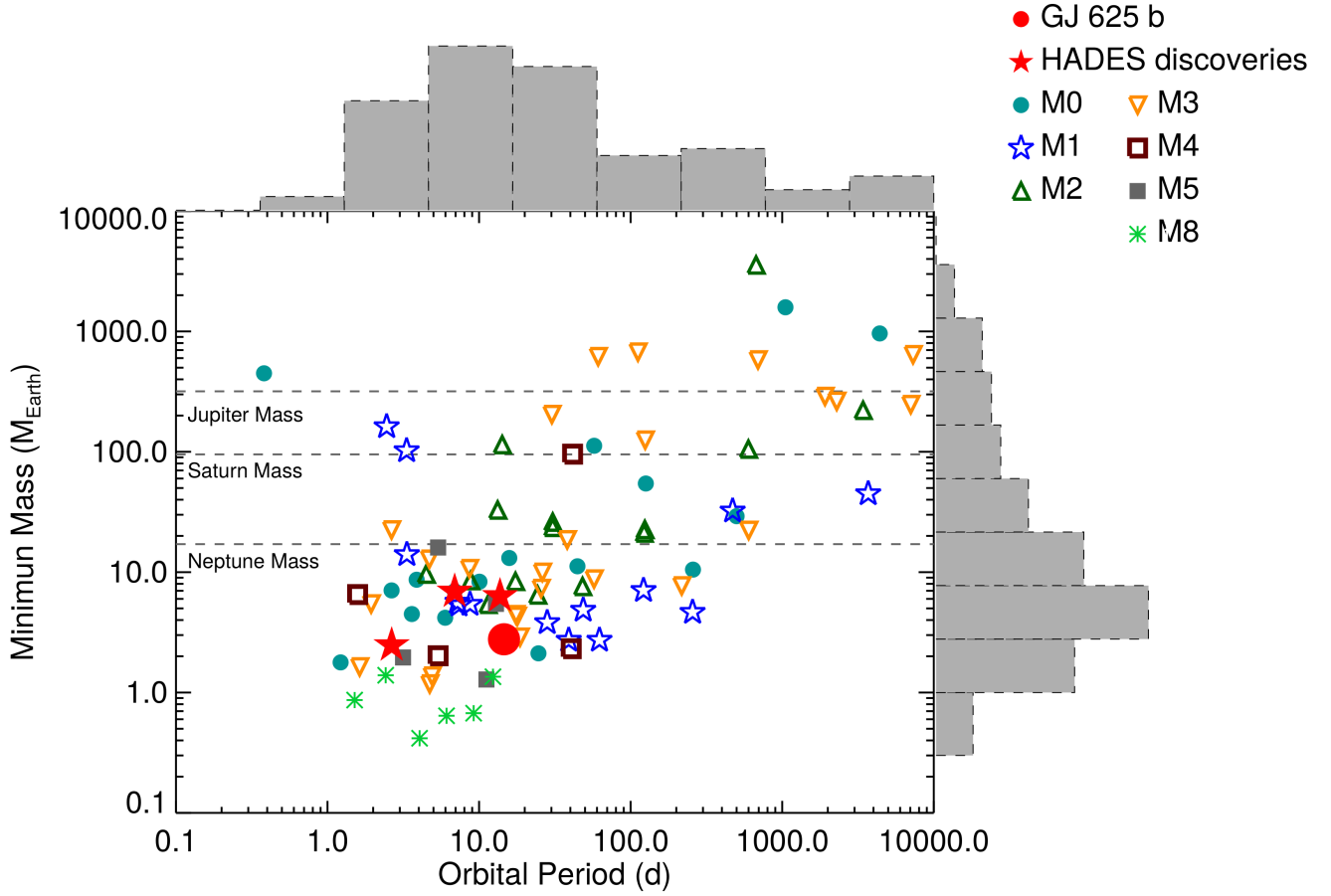


Fig. 21: Minimum mass versus orbital period for the known planets with determined masses around M-dwarf stars (using data from exoplanet.eu) divided by the spectral type of the host star. The red filled dot shows the position of GJ 625 b, and the red filled stars show the position of GJ 3998 b, c and GJ 3942 b (Affer et al. 2016; Perger et al. 2017b). Horizontal dashed lines show the mass of the solar system planets for comparison. On the edges of the figure the distribution for each parameter is shown.

- Ribas, I., Bolmont, E., Selsis, F., et al. 2016, *A&A*, 596, A111  
Robertson, P., Endl, M., Cochran, W. D., & Dodson-Robinson, S. E. 2013, *ApJ*, 764, 3  
Robertson, P., Mahadevan, S., Endl, M., & Roy, A. 2014, *Science*, 345, 440  
Saar, S. H. & Donahue, R. A. 1997, *ApJ*, 485, 319  
Scandariato, G., Maldonado, J., Affer, L., et al. 2017, *A&A*, 598, A28  
Scargle, J. D. 1982, *ApJ*, 263, 835  
Selsis, F., Kasting, J. F., Levrard, B., et al. 2007, *A&A*, 476, 1373  
Suárez Mascareño, A., González Hernández, J. I., Rebolo, R., et al. 2017a, *A&A*, 597, A108  
Suárez Mascareño, A., Rebolo, R., & González Hernández, J. I. 2016, *A&A*, 595, A12  
Suárez Mascareño, A., Rebolo, R., González Hernández, J. I., & Esposito, M. 2015, *MNRAS*, 452, 2745  
Suárez Mascareño, A., Rebolo, R., González Hernández, J. I., & Esposito, M. 2017b, *ArXiv e-prints* [arXiv:1703.08884]  
Udry, S., Bonfils, X., Delfosse, X., et al. 2007, *A&A*, 469, L43  
van Leeuwen, F. 2007, *A&A*, 474, 653  
Vanderburg, A., Plavchan, P., Johnson, J. A., et al. 2016, *MNRAS*, 459, 3565  
Velasco, S., Rebolo, R., Oscoz, A., et al. 2016, *MNRAS*, 460, 3519  
Vidotto, A. A., Jardine, M., Morin, J., et al. 2013, *A&A*, 557, A67  
Waldmeier, M. 1961, *The sunspot-activity in the years 1610-1960*  
Wargelin, B. J., Saar, S. H., Pojmański, G., Drake, J. J., & Kashyap, V. L. 2017, *MNRAS*, 464, 3281  
Wildi, F., Pepe, F., Chazelas, B., Lo Curto, G., & Lovis, C. 2010, in *SPIE*, Vol. 7735, *Ground-based and Airborne Instrumentation for Astronomy III*, 77354X  
Winn, J. N. 2010, *ArXiv e-prints* [arXiv:1001.2010]  
Wright, D. J., Wittenmyer, R. A., Tinney, C. G., Bentley, J. S., & Zhao, J. 2016, *ApJ*, 817, L20  
Zechmeister, M. & Kürster, M. 2009, *A&A*, 496, 577  
Zuluaga, J. I., Bustamante, S., Cuartas, P. A., & Hoyos, J. H. 2013, *ApJ*, 770, 23

## Appendix A: Full dataset

Table A.1: Full available dataset. Radial velocities are given in the Barycentric Reference Frame after subtracting the secular acceleration. Radial-velocity uncertainties include photon noise, calibration and telescope related uncertainties. BJD is referenced to day 2450000,  $\langle V_{r\ CCF} \rangle = 12850.11\ \text{ms}^{-1}$ ,  $\langle \text{FWHM} \rangle = 3703.09\ \text{ms}^{-1}$ .

BJD (d)	$\Delta V_{r\ CCF}$ ( $\text{ms}^{-1}$ )	$\sigma V_{r\ CCF}$ ( $\text{ms}^{-1}$ )	$\Delta V_{r\ TERRA}$ ( $\text{ms}^{-1}$ )	$\sigma V_{r\ TERRA}$ ( $\text{ms}^{-1}$ )	$\Delta \text{FWHM}$ ( $\text{ms}^{-1}$ )	BIS Span ( $\text{ms}^{-1}$ )	$S_{MW}$	$\sigma S_{MW}$	$H_\alpha$	$\sigma H_\alpha$
6438.576	2.00	1.31	2.64	1.19	-2.48	-7.68	0.620	0.009	0.4260	0.0006
6440.577	-2.63	1.25	-0.22	1.25	1.77	-6.84	0.627	0.008	0.4164	0.0005
6441.698	-0.08	1.33	1.63	1.31	-0.82	-8.32	0.623	0.008	0.4210	0.0005
6442.513	-0.88	1.21	-0.83	1.22	5.56	-8.24	0.728	0.008	0.4300	0.0005
6443.481	-1.17	1.52	-0.33	1.34	-1.57	-4.93	0.654	0.012	0.4157	0.0008
6484.636	-5.47	1.65	-4.33	1.33	2.81	-11.65	0.529	0.011	0.4124	0.0008
6485.458	-4.32	1.30	-4.40	1.21	-2.18	-10.24	0.595	0.008	0.4137	0.0005
6507.464	2.71	2.10	2.98	1.90	-6.48	-12.12	0.553	0.013	0.4069	0.0009
6533.354	-0.90	1.29	0.67	1.25	1.38	-8.02	0.614	0.008	0.4187	0.0005
6534.363	-4.75	1.65	-2.98	1.38	-5.46	-7.17	0.601	0.012	0.4221	0.0008
6535.419	-0.21	1.45	-0.49	1.29	-0.76	-6.18	0.592	0.012	0.4141	0.0008
6536.475	-0.84	1.29	1.26	1.27	-2.85	-8.30	0.684	0.008	0.4143	0.0005
6693.714	-2.83	1.51	-1.58	1.39	0.19	-5.41	0.744	0.013	0.4199	0.0007
6694.738	-2.29	1.46	-1.86	1.38	1.60	-10.44	0.721	0.012	0.4175	0.0007
6695.707	3.72	2.04	5.27	1.52	-0.13	-6.90	0.663	0.017	0.4140	0.0010
6696.698	-1.52	1.53	0.97	1.30	2.95	-5.39	0.692	0.012	0.4170	0.0007
6697.710	1.71	1.28	3.68	1.25	3.28	-7.19	0.821	0.011	0.4309	0.0006
6698.711	0.93	1.61	2.22	1.37	0.84	-4.92	0.663	0.013	0.4203	0.0008
6700.690	-0.65	1.31	0.92	1.26	1.72	-6.98	0.792	0.011	0.4158	0.0006
6701.667	3.17	1.46	4.74	1.33	-5.70	-3.22	0.717	0.013	0.4161	0.0008
6702.662	-1.44	1.45	1.79	1.43	-4.22	-6.69	0.769	0.011	0.4278	0.0007
6775.629	1.08	1.75	2.53	1.39	2.65	-10.16	0.779	0.016	0.4069	0.0010
6783.490	3.03	1.32	3.46	1.31	5.21	-7.24	0.818	0.012	0.4229	0.0007
6784.494	0.99	1.30	1.62	1.20	6.69	-4.60	0.857	0.011	0.4262	0.0006
6798.430	-1.74	1.29	-0.87	1.22	0.89	-6.52	0.815	0.010	0.4233	0.0006
6799.453	0.95	1.28	1.36	1.23	-0.99	-6.34	0.833	0.011	0.4266	0.0006
6800.417	0.31	1.41	3.22	1.29	2.46	-5.21	0.894	0.013	0.4371	0.0007
6821.485	-2.71	1.84	-3.05	1.51	-7.94	-4.35	0.590	0.016	0.4217	0.0011
6854.495	-1.17	1.25	0.21	1.25	-1.00	-5.66	0.931	0.011	0.4235	0.0006
6855.484	-1.44	1.32	-0.18	1.25	-0.89	-7.25	0.746	0.011	0.4091	0.0006
6857.467	-0.71	1.29	0.15	1.21	3.35	-4.95	0.813	0.012	0.4049	0.0007
6858.436	-0.09	1.35	1.39	1.29	4.39	-7.70	0.777	0.011	0.4093	0.0006
6859.458	4.93	1.32	4.60	1.28	3.63	-9.58	0.761	0.010	0.4075	0.0006
6860.423	2.78	1.24	3.02	1.17	4.26	-6.83	0.845	0.010	0.4127	0.0006
6861.450	2.21	1.27	4.23	1.24	7.78	-5.48	0.994	0.011	0.4216	0.0005
6877.444	2.30	1.30	3.25	1.19	2.60	-8.93	0.813	0.011	0.4292	0.0006
6878.442	2.18	1.23	2.98	1.25	4.06	-5.39	0.781	0.010	0.4154	0.0005
6879.383	-1.02	1.24	-0.29	1.19	6.14	-4.11	0.889	0.012	0.4259	0.0006
6880.386	1.05	1.36	2.13	1.25	4.76	-3.22	0.781	0.012	0.4214	0.0007
6881.403	0.84	1.95	0.81	1.47	-1.91	-6.34	0.793	0.020	0.4276	0.0011
6892.395	1.44	1.31	2.62	1.21	-0.40	-7.09	0.736	0.011	0.4132	0.0006
6893.398	3.93	1.45	2.50	1.29	3.29	-6.48	0.711	0.012	0.4140	0.0007
6894.401	2.30	1.39	1.50	1.30	2.56	-6.94	0.716	0.010	0.4088	0.0006
6897.410	-2.36	1.29	-1.97	0.98	-0.59	-3.46	0.757	0.015	0.4259	0.0009
6898.381	-4.20	1.39	-1.51	1.07	-1.21	-7.39	0.791	0.015	0.4251	0.0009
6899.395	-0.69	1.26	0.34	0.98	-4.95	-0.65	0.734	0.017	0.4186	0.0010
6904.495	-2.25	1.01	-0.90	0.90	-2.00	-6.76	0.760	0.009	0.4263	0.0006
6905.388	1.03	0.99	1.21	0.94	-6.51	-4.09	0.767	0.011	0.4209	0.0006
6907.382	-2.05	1.02	-0.46	0.92	-10.51	-5.15	0.694	0.010	0.4182	0.0006
6909.380	-4.11	1.23	-2.25	1.24	-7.44	-4.52	0.707	0.009	0.4196	0.0006
6918.389	-3.37	1.48	-3.10	1.18	-8.96	-7.26	0.595	0.013	0.4138	0.0009
6920.388	-2.44	1.09	-1.45	0.93	-13.49	-10.08	0.670	0.010	0.4172	0.0007
6921.393	-1.43	1.78	-1.85	1.38	-15.38	-6.81	0.658	0.016	0.4167	0.0010
6932.342	-1.54	1.45	-1.60	1.26	-5.48	-9.18	0.706	0.016	0.4190	0.0010
6938.320	-1.49	1.08	0.61	0.97	-1.03	-7.88	0.779	0.012	0.4142	0.0007
6940.320	-0.47	1.16	-0.94	1.36	-0.26	-5.09	0.830	0.013	0.4176	0.0007
6942.318	1.43	0.93	1.41	0.90	4.59	-6.06	0.909	0.010	0.4208	0.0005

Table A.1: Full available dataset. Radial velocities are given in the Barycentric Reference Frame after subtracting the secular acceleration. Radial-velocity uncertainties include photon noise, calibration and telescope related uncertainties. BJD is referenced to day 2450000,  $\langle V_{r\ CCF} \rangle = 12850.11\ \text{ms}^{-1}$ ,  $\langle \text{FWHM} \rangle = 3703.09\ \text{ms}^{-1}$ .

BJD (d)	$\Delta V_{r\ CCF}$ ( $\text{ms}^{-1}$ )	$\sigma V_{r\ CCF}$ ( $\text{ms}^{-1}$ )	$\Delta V_{r\ TERRA}$ ( $\text{ms}^{-1}$ )	$\sigma V_{r\ TERRA}$ ( $\text{ms}^{-1}$ )	$\Delta \text{FWHM}$ ( $\text{ms}^{-1}$ )	BIS Span ( $\text{ms}^{-1}$ )	$S_{MW}$	$\sigma S_{MW}$	$H_\alpha$	$\sigma H_\alpha$
6943.315	1.45	1.07	0.40	0.95	4.47	-5.65	0.831	0.012	0.4140	0.0006
7113.565	-3.73	1.63	-2.42	1.41	-7.34	-2.10	0.773	0.017	0.4062	0.0009
7114.622	-5.75	3.47	-3.72	2.51	-4.94	-10.36	0.769	0.034	0.4065	0.0019
7115.529	-2.29	1.58	-2.15	1.30	-9.84	-5.27	0.629	0.013	0.4031	0.0008
7116.576	-2.83	1.26	-1.73	1.18	-4.91	-5.72	0.660	0.009	0.4038	0.0005
7123.548	2.42	3.67	1.08	2.45	0.81	-6.15	0.607	0.032	0.4107	0.0022
7137.713	2.10	1.36	5.33	1.35	-6.38	-7.25	0.676	0.009	0.4073	0.0005
7139.674	4.80	1.44	3.90	1.29	-3.61	-5.28	0.650	0.011	0.4055	0.0007
7142.604	-0.34	1.36	0.45	1.25	-2.94	-3.25	0.720	0.012	0.4117	0.0007
7143.549	-1.32	1.53	-2.04	1.35	-1.85	-6.11	0.615	0.013	0.4071	0.0008
7144.543	0.95	1.52	1.87	1.35	-5.68	-7.39	0.760	0.015	0.4243	0.0009
7239.410	1.79	1.01	0.90	0.95	-1.23	-7.22	0.761	0.010	0.4157	0.0006
7240.410	5.76	1.03	6.15	0.95	0.21	-4.99	0.726	0.011	0.4135	0.0006
7241.407	0.71	1.30	2.84	1.09	-5.87	-9.06	0.723	0.013	0.4145	0.0008
7242.407	2.13	1.28	3.25	1.05	-4.76	-4.11	0.755	0.014	0.4269	0.0008
7249.438	-1.31	1.35	-2.59	1.19	1.21	-5.66	0.742	0.015	0.4135	0.0009
7251.395	-0.40	0.99	-1.04	0.87	2.22	-5.80	0.798	0.011	0.4209	0.0006
7260.370	-0.84	0.94	-0.84	0.90	-0.80	-4.44	0.777	0.010	0.4146	0.0006
7261.379	0.84	1.05	-0.59	1.06	1.46	-7.19	0.754	0.011	0.4099	0.0006
7262.376	-0.36	1.04	-0.47	0.92	3.59	-3.07	0.803	0.012	0.4212	0.0007
7263.376	1.33	1.00	1.77	0.95	3.34	-8.43	0.839	0.011	0.4176	0.0006
7264.375	-0.40	1.34	-0.34	1.01	7.63	-3.16	0.826	0.016	0.4247	0.0009
7274.359	0.22	1.16	-0.10	0.93	1.28	-5.93	0.739	0.011	0.4018	0.0007
7275.359	-1.41	1.43	-1.71	1.39	4.38	-6.65	0.765	0.012	0.4069	0.0007
7276.358	-2.44	1.05	-3.20	0.95	7.00	-6.61	0.946	0.013	0.4176	0.0007
7277.356	-3.46	1.02	-3.28	1.03	5.83	-2.72	0.769	0.011	0.4045	0.0006
7282.371	2.91	0.96	5.24	1.49	3.05	-5.72	0.757	0.010	0.4013	0.0005
7285.373	0.59	1.27	-0.99	1.14	4.22	-5.68	0.642	0.011	0.4093	0.0007
7286.357	-0.47	1.09	-0.74	0.97	-1.80	-4.13	0.685	0.011	0.4050	0.0007
7287.359	3.16	1.10	3.46	0.98	0.28	-5.95	0.673	0.010	0.4070	0.0007
7293.358	0.08	1.42	-1.26	1.32	0.14	-6.87	0.731	0.012	0.4110	0.0007
7296.390	2.53	1.14	3.24	1.18	-1.87	-11.83	0.664	0.008	0.4146	0.0006
7443.689	3.02	2.09	2.59	1.47	-1.82	-5.43	0.561	0.017	0.4027	0.0011
7472.703	3.78	1.57	4.04	1.39	-5.03	-7.27	0.702	0.015	0.4161	0.0009
7474.665	6.60	1.40	5.81	1.28	-0.61	-2.85	0.671	0.011	0.4117	0.0007
7502.703	-0.82	1.38	-0.55	1.36	-8.39	-6.57	0.609	0.010	0.4148	0.0007
7508.527	-4.00	1.11	-1.33	1.00	-2.50	-7.08	0.703	0.009	0.4204	0.0006
7508.659	-2.13	1.50	0.54	1.44	-2.49	-12.67	0.679	0.011	0.4170	0.0007
7509.550	-6.62	1.49	-7.26	1.30	-1.09	-11.35	0.756	0.012	0.4202	0.0008
7510.531	-3.39	1.44	-3.98	1.19	-4.10	-8.28	0.681	0.011	0.4141	0.0007
7513.622	-3.47	1.52	-4.33	1.31	-2.63	-7.93	0.696	0.013	0.4148	0.0008
7521.524	-2.78	1.46	-1.79	1.25	-4.16	-4.58	0.788	0.013	0.4094	0.0007
7522.497	0.28	1.42	-0.78	1.37	0.43	-5.13	0.725	0.013	0.4071	0.0007
7523.494	-1.30	1.84	-1.64	1.41	0.56	-7.26	0.676	0.017	0.4083	0.0010
7524.495	-1.60	1.76	-0.93	1.60	4.52	-9.77	0.719	0.015	0.4090	0.0009
7525.521	-3.43	1.62	-3.72	1.27	10.84	-9.65	0.963	0.017	0.4281	0.0009
7535.641	-3.44	1.38	-4.24	1.15	3.99	-11.65	0.782	0.014	0.4101	0.0008
7536.504	-0.46	1.32	1.46	1.02	6.61	-4.87	0.802	0.014	0.4090	0.0008
7537.496	-0.19	1.56	-0.35	1.23	8.41	-1.00	0.973	0.020	0.4306	0.0010
7537.611	0.95	1.22	-1.19	1.24	6.29	-5.58	0.881	0.013	0.4135	0.0007
7538.489	-0.15	1.06	-0.73	1.00	2.95	-7.15	0.860	0.010	0.4218	0.0006
7538.620	-0.05	1.15	-0.16	1.02	4.42	-8.91	0.839	0.010	0.4101	0.0006
7540.658	-2.09	1.31	0.11	1.04	3.40	-10.09	0.724	0.012	0.4062	0.0007
7549.591	7.97	1.35	8.69	1.25	-3.93	-11.09	0.747	0.010	0.4118	0.0007
7550.597	5.93	1.23	6.33	1.11	5.35	-9.50	0.727	0.009	0.4206	0.0006
7551.582	0.78	1.48	-0.33	1.09	-1.05	-7.63	0.614	0.012	0.4151	0.0008
7552.554	-0.39	1.26	0.62	1.07	-0.11	-7.40	0.632	0.011	0.4142	0.0007
7553.561	-2.19	1.43	-1.69	1.21	-0.30	-6.43	0.655	0.013	0.4142	0.0009

Table A.1: Full available dataset. Radial velocities are given in the Barycentric Reference Frame after subtracting the secular acceleration. Radial-velocity uncertainties include photon noise, calibration and telescope related uncertainties. BJD is referenced to day 2450000,  $\langle V_{r\ CCF} \rangle = 12850.11\ \text{ms}^{-1}$ ,  $\langle \text{FWHM} \rangle = 3703.09\ \text{ms}^{-1}$ .

BJD (d)	$\Delta V_{r\ CCF}$ ( $\text{ms}^{-1}$ )	$\sigma V_{r\ CCF}$ ( $\text{ms}^{-1}$ )	$\Delta V_{r\ TERRA}$ ( $\text{ms}^{-1}$ )	$\sigma V_{r\ TERRA}$ ( $\text{ms}^{-1}$ )	$\Delta \text{FWHM}$ ( $\text{ms}^{-1}$ )	BIS Span ( $\text{ms}^{-1}$ )	$S_{MW}$	$\sigma S_{MW}$	$H_\alpha$	$\sigma H_\alpha$
7594.464	0.13	1.51	-0.26	1.35	1.00	-5.21	0.817	0.012	0.4181	0.0007
7596.458	0.77	1.52	-0.48	1.45	1.47	-5.79	0.761	0.014	0.4188	0.0008
7597.470	1.36	1.53	0.71	1.43	1.71	-10.35	0.702	0.012	0.4167	0.0007
7603.456	-0.63	1.36	0.19	1.32	7.67	-8.98	0.757	0.009	0.4093	0.0006
7604.446	-0.13	1.61	-0.43	1.43	9.40	-6.31	0.779	0.014	0.4111	0.0008
7606.393	4.30	1.47	1.86	1.19	10.04	-5.10	0.765	0.014	0.4124	0.0008
7607.474	5.68	2.20	5.39	2.23	16.25	-7.92	0.763	0.018	0.4103	0.0011
7608.435	0.46	1.12	-0.90	1.02	9.23	-6.53	0.802	0.011	0.4103	0.0006
7609.430	-1.96	3.14	-2.40	2.19	13.38	-7.73	0.817	0.030	0.4128	0.0018
7610.400	0.15	2.67	0.40	2.15	8.52	-7.85	0.983	0.031	0.4348	0.0016
7620.430	1.97	1.68	0.52	1.45	-0.40	-6.87	0.668	0.015	0.4125	0.0009
7621.461	1.71	2.81	-0.53	1.80	11.63	-12.30	0.436	0.018	0.4147	0.0015
7625.405	0.43	1.02	-0.33	1.10	-4.17	-4.94	0.815	0.011	0.4158	0.0006
7626.409	0.61	1.38	0.20	1.18	-5.01	-6.14	0.710	0.014	0.4111	0.0009
7627.403	-1.73	1.22	0.86	1.06	-6.58	-4.51	0.687	0.013	0.4175	0.0008
7628.406	-1.25	1.21	-1.71	1.13	-5.40	-3.69	0.814	0.011	0.4267	0.0007
7629.402	2.80	1.15	2.58	1.01	-0.81	-7.01	0.700	0.012	0.4179	0.0007
7632.404	-0.48	1.09	-0.26	0.98	-6.03	-6.18	0.744	0.011	0.4084	0.0006
7637.400	3.40	1.15	2.82	1.09	-5.64	-7.31	0.653	0.010	0.4186	0.0007
7638.385	1.80	1.16	1.54	1.12	-5.09	-8.60	0.676	0.012	0.4173	0.0008
7641.383	-0.89	1.00	-1.85	1.02	-5.71	-7.20	0.650	0.009	0.4261	0.0006
7642.382	-2.00	1.07	-2.65	1.03	-3.46	-4.29	0.627	0.010	0.4199	0.0007
7643.380	-1.43	1.15	-2.24	1.09	-4.58	-5.93	0.689	0.012	0.4283	0.0007
7645.381	-1.98	1.18	-1.15	1.16	-7.10	-8.70	0.640	0.011	0.4276	0.0007
7646.377	-1.07	1.14	-1.08	0.98	-5.02	-7.60	0.670	0.011	0.4161	0.0007

Table A.2: EXORAP B band photometric dataset

MJD (d)	$\Delta m_B$ (mmag)	$\sigma m_B$ (mmag)
6782.913	29.78	10.13
6784.956	30.38	10.10
6786.940	28.48	10.11
6797.895	19.68	10.14
6798.910	18.58	10.11
6801.896	30.18	10.11
6802.888	30.78	10.11
6813.872	26.58	10.10
6817.853	22.18	10.13
6830.982	9.68	10.13
6834.832	10.38	10.16
6835.832	9.68	10.11
6836.832	10.08	10.11
6839.823	0.58	10.11
6840.822	11.48	10.13
6841.822	6.38	10.20
6845.876	4.28	10.16
6851.846	20.38	10.13
6866.853	27.68	10.10
6868.852	21.48	10.10
7037.086	-0.92	10.11
7110.987	4.38	10.13
7112.016	-3.82	10.10
7113.014	1.68	10.10
7117.946	16.18	10.10
7154.924	20.78	10.07
7162.053	13.78	10.06
7165.006	31.08	10.06
7165.970	14.48	10.05
7171.845	8.18	10.06
7176.994	-0.22	10.07
7184.862	8.28	10.08
7196.035	2.18	10.02
7199.824	4.38	10.05
7200.864	5.28	10.04
7204.069	-8.42	10.04
7208.096	-27.02	10.08
7208.919	-19.02	10.05
7209.918	-14.72	10.03
7211.064	-26.02	10.05
7211.912	-13.12	10.03
7212.913	-14.62	10.04
7214.925	-9.82	10.03
7216.057	-24.32	10.03
7222.052	-23.82	10.08
7222.963	-12.92	10.05
7224.958	-9.02	10.04
7225.955	-11.42	10.03
7227.897	-6.52	10.04
7231.864	4.88	10.03
7232.948	6.18	10.04
7239.991	-16.52	10.08
7240.984	-12.22	10.06
7247.969	0.28	10.07
7258.951	5.28	10.06
7386.203	2.38	10.04
7398.172	-3.22	10.04
7416.127	-7.52	10.04
7417.128	-4.72	10.04

Table A.2: EXORAP B band photometric dataset (continued)

MJD (d)	$\Delta m_B$ (mmag)	$\sigma m_B$ (mmag)
7419.097	-10.72	10.04
7424.121	-6.42	10.04
7425.115	-4.02	10.06
7437.081	-5.32	10.04
7439.068	-9.32	10.07
7440.054	-8.52	10.06
7443.055	1.78	10.10
7445.055	9.78	10.11
7455.091	6.38	10.05
7483.003	0.78	10.06
7483.998	0.48	10.07
7488.014	1.78	10.05
7488.995	7.68	10.05
7489.993	7.48	10.06
7490.987	-0.82	10.07
7491.988	1.38	10.08
7493.979	2.18	10.06
7494.957	-2.12	10.07
7495.949	6.88	10.10
7497.936	-3.12	10.06
7498.922	-8.52	10.10
7504.949	-7.32	10.05
7507.953	-6.12	10.05
7511.993	-5.12	10.05
7515.073	-12.12	10.08
7517.002	-8.52	10.11
7518.027	-3.92	10.05
7523.995	-1.02	10.05
7524.922	12.78	10.06
7545.962	-4.02	10.06
7546.958	1.48	10.06
7550.949	-2.82	10.08
7552.965	-7.42	10.06
7553.904	1.48	10.06
7554.847	-2.92	10.07
7565.945	-11.72	10.06
7569.959	-11.12	10.08
7570.957	-9.22	10.08
7571.956	-17.82	10.06
7573.957	-10.12	10.06
7574.957	-8.02	10.08
7575.990	-13.42	10.08
7576.989	-12.32	10.06
7577.987	-13.62	10.08
7578.987	-19.92	10.10
7590.945	-11.42	10.10
7591.949	-24.12	10.11
7593.977	-17.82	10.10
7746.197	-10.02	10.07



Table A.3: EXORAP V band photometric dataset

MJD (d)	$\Delta m_V$ (mmag)	$\sigma m_V$ (mmag)
6782.914	25.43	10.05
6784.957	21.23	10.04
6785.950	22.23	10.08
6786.941	40.13	10.05
6787.862	26.33	10.06
6797.896	10.63	10.06
6798.912	29.03	10.05
6801.897	14.23	10.05
6802.889	10.63	10.05
6812.873	14.03	10.04
6816.832	4.43	10.05
6830.983	-4.37	10.05
6832.849	-4.67	10.07
6834.833	4.23	10.06
6835.833	1.03	10.05
6836.833	1.83	10.05
6839.824	-10.77	10.05
6840.824	2.23	10.06
6841.824	-3.47	10.07
6842.823	-11.57	10.08
6845.877	0.23	10.07
6851.848	8.83	10.05
6863.041	2.73	10.06
6866.854	14.63	10.05
6868.853	16.33	10.05
7037.087	3.63	10.05
7112.017	-6.57	10.04
7113.015	-6.97	10.04
7117.947	2.93	10.04
7154.925	-7.87	10.03
7165.008	0.93	10.02
7184.863	-21.77	10.03
7196.036	-1.07	10.02
7199.825	-0.07	10.06
7200.865	-1.97	10.02
7204.070	-8.67	10.02
7208.097	-16.47	10.03
7208.920	-12.27	10.02
7211.065	-15.87	10.02
7211.913	-15.87	10.02
7222.054	-14.87	10.04
7222.964	-15.07	10.02
7231.865	-3.27	10.02
7239.992	-1.67	10.05
7240.985	1.63	10.04
7247.970	1.43	10.04
7258.952	5.03	10.04
7386.204	6.73	10.03
7398.173	9.33	10.03
7416.128	-0.77	10.03
7417.129	-3.87	10.03
7419.098	-3.57	10.03
7424.122	4.43	10.03
7425.116	2.43	10.05
7437.082	1.93	10.03
7439.069	-5.77	10.05
7440.055	-1.57	10.04
7445.056	7.43	10.03

Table A.3: EXORAP V band photometric dataset (continued)

MJD (d)	$\Delta m_V$ (mmag)	$\sigma m_V$ (mmag)
7455.092	4.23	10.03
7483.004	-0.57	10.04
7483.999	0.93	10.04
7488.015	8.13	10.03
7488.996	2.53	10.03
7489.993	-4.37	10.04
7490.988	-2.77	10.06
7491.989	-5.17	10.06
7493.979	7.63	10.05
7495.950	0.83	10.07
7497.937	-6.27	10.05
7498.923	-2.57	10.06
7504.950	-1.67	10.04
7507.954	-7.77	10.05
7511.994	-3.17	10.04
7515.073	-0.07	10.06
7517.003	-5.67	10.08
7518.027	0.63	10.04
7523.996	7.13	10.04
7524.923	10.03	10.07
7538.970	9.43	10.14
7545.963	-4.77	10.07
7546.959	1.83	10.07
7550.950	-3.37	10.14
7552.966	-2.47	10.07
7554.848	-3.97	10.08
7565.945	-8.97	10.08
7569.959	-8.87	10.10
7570.958	-5.47	10.11
7571.957	-7.07	10.08
7573.958	-9.47	10.08
7574.957	-10.07	10.10
7575.990	-8.97	10.10
7576.990	-15.67	10.08
7577.988	-10.17	10.11
7578.988	-12.77	10.13
7590.946	-5.07	10.10
7591.949	-0.77	10.13
7593.978	-4.87	10.11
7746.198	-7.77	10.08

Table A.4: EXORAP R band photometric dataset

MJD (d)	$\Delta m_V$ (mmag)	$\sigma m_V$ (mmag)
6782.915	36.87	10.05
6784.957	42.47	10.04
6785.951	34.37	10.08
6786.941	44.07	10.04
6787.863	45.67	10.06
6798.912	45.77	10.05
6802.890	30.27	10.05
6830.984	21.57	10.05
6832.849	17.57	10.07
6834.834	20.47	10.08
6835.834	18.17	10.05
6839.825	17.57	10.05
6841.824	12.17	10.08
6845.878	22.17	10.07
6851.848	27.07	10.05
6863.042	9.17	10.06
7037.088	1.67	10.05
7112.017	3.17	10.03
7113.016	-11.23	10.04
7117.947	-8.23	10.03
7154.925	-4.53	10.03
7165.008	5.67	10.02
7184.863	-8.83	10.03
7196.037	-3.13	10.02
7199.826	-5.83	10.03
7200.866	-1.93	10.02
7204.071	-19.03	10.02
7208.098	-34.83	10.02
7211.065	-17.73	10.02
7222.054	-29.33	10.02
7231.866	-5.13	10.02
7239.992	-5.83	10.05
7240.985	-10.53	10.04
7247.970	-12.63	10.05
7258.953	-1.73	10.05
7386.204	-0.33	10.04
7398.173	0.17	10.04
7416.129	-14.53	10.04
7417.129	-10.33	10.04
7419.098	-8.53	10.04
7424.123	-9.73	10.04
7425.117	-9.03	10.06
7437.082	-0.53	10.04
7439.069	-4.03	10.05
7440.056	-3.03	10.05
7445.056	1.17	10.04
7455.093	-4.13	10.04
7483.004	-2.13	10.05
7483.999	-1.23	10.06
7488.016	12.77	10.04
7488.996	-7.33	10.04
7489.994	-3.53	10.05
7490.989	-5.03	10.06
7491.990	-7.73	10.06
7493.980	-7.13	10.05
7495.950	-7.33	10.06
7497.938	-8.43	10.05
7498.923	-15.43	10.05
7504.950	-6.03	10.04
7507.955	-9.93	10.04

Table A.4: EXORAP R band photometric dataset (continued)

MJD (d)	$\Delta m_V$ (mmag)	$\sigma m_V$ (mmag)
7511.994	-8.33	10.04
7515.074	-17.83	10.06
7517.003	-14.53	10.08
7518.028	-5.63	10.04
7524.923	10.47	10.08
7538.970	-4.53	10.13
7545.963	-3.13	10.10
7546.959	0.67	10.10
7552.966	0.87	10.10
7554.848	6.37	10.13
7565.946	4.57	10.11
7569.960	-13.13	10.14
7570.958	-5.33	10.14
7571.957	-18.33	10.11
7573.958	-7.23	10.11
7574.958	-14.33	10.14
7575.991	-22.83	10.14
7576.990	-6.63	10.11
7578.988	0.97	10.16
7590.946	-4.83	10.13
7593.978	-13.23	10.14
7746.198	-8.33	10.08

Table A.5: EXORAP I band photometric dataset

MJD (d)	$\Delta m_V$ (mmag)	$\sigma m_V$ (mmag)
6782.915	35.96	10.04
6784.958	40.26	10.04
6785.951	37.16	10.05
6787.863	38.66	10.05
6798.913	58.66	10.04
6830.984	31.76	10.04
6832.850	24.86	10.07
6835.834	23.76	10.04
6839.825	19.06	10.04
6841.825	20.46	10.06
6845.878	29.56	10.06
6851.849	38.66	10.04
6868.854	34.26	10.04
7031.104	-17.34	10.04
7037.088	-23.14	10.03
7112.018	-25.54	10.03
7113.016	-21.34	10.03
7117.948	-12.24	10.02
7154.926	-24.94	10.02
7165.009	-12.94	10.02
7196.037	-14.74	10.01
7199.826	-11.94	10.03
7231.866	-11.04	10.01
7239.992	13.56	10.05
7240.985	-5.44	10.03
7247.971	16.06	10.04
7386.204	-14.34	10.02
7398.173	-4.94	10.03
7416.129	-1.74	10.03
7417.129	-25.14	10.03
7419.099	3.26	10.03
7424.123	-21.94	10.03
7425.117	-11.64	10.04
7437.082	-14.94	10.03
7439.069	-12.54	10.03
7445.056	4.66	10.05
7455.093	-12.94	10.05
7483.004	-2.44	10.06
7484.000	-9.24	10.07
7488.016	-5.04	10.05
7488.997	-12.64	10.05
7489.994	-12.94	10.06
7490.989	-7.14	10.07
7491.990	-2.24	10.08
7493.980	-17.04	10.06
7495.950	-3.34	10.07
7497.938	-17.24	10.06
7498.923	-20.04	10.06
7504.951	-18.94	10.05
7507.955	-13.44	10.05
7511.994	-8.34	10.05
7515.074	-13.34	10.07
7517.004	-2.94	10.10
7518.028	-9.44	10.06
7523.996	6.16	10.05